



מכון ויצמן למדע  
WEIZMANN INSTITUTE OF SCIENCE

Thesis for the degree  
Master of Science

עבודת גמר (תזה) לתואר  
מוסמך למדעים

Submitted to the Scientific Council of the  
Weizmann Institute of Science  
Rehovot, Israel

מוגשת למועצה המדעית של  
מכון ויצמן למדע  
רחובות, ישראל

By  
Tom Manovitz

מאת  
תום מנוביץ'

Individual Addressing and  
Imaging of Ions in a Paul  
Trap

Advisor: Prof. Roee Ozeri

מנחה: פרופ' רועי עוזרי

March 2016

אדר תשע"ו

## **Acknowledgements**

There is no shortage of people that deserve recognition for the completion of this work. I arrived at the ion trapping group with almost no theoretical or practical knowledge relevant to the project I was about to undertake, and not an idea of the hurdles I would need to overcome in order to bring it to completion. The remedy to my ignorance was the gracious and exceedingly patient support of my fellow group members. It would hardly be an exaggeration to claim that every single day of my work in the past year included at least some discussion with and advice from my coworkers. For this, as well as their friendliness, fine character and general good will, I would like to thank Ziv Meir, Tomas Sikorsky, Ruti Ben Shlomi, Meir Alon, Nitzan Ackerman, Yotam Shapira and Ravid Shaniv. Furthermore, I would like to thank the last two for the countless hours spent with me in the lab; the existence of this thesis is a direct result of their perseverance and intelligence. I want to thank Gershon Elazar, Yosef Shopen and Guy Han for the planning and construction of the mechanical elements of the system, done swiftly, precisely and professionally. Finally, I want to thank my advisor Roe Ozeri for his unwavering support, wise advice, and mentoring, always given generously and with a smile.

## Abstract

The following thesis reports on the construction and characterization of a module for imaging and individual addressing of  $^{88}\text{Sr}^+$  ions held in a linear Paul trap. Prior to the module construction state detection was ambivalent and single addressing was performed on two ions in a non-scalable fashion. The detection ambivalence is solved by spatially resolving the ions, achieved by imaging the ion register onto an EMCCD camera and using the image to determine register state. Scalable single addressing is done by tightly focusing an addressing laser beam to  $3.00\ \mu\text{m}$  FWHM of the field amplitude onto the ion chain, and spatially steering the beam with two acousto-optic deflectors set in an XY configuration. For a  $1\ \text{msec}$  detection, and an inter-ion distance larger than  $1.9\ \mu\text{m}$ , we report a detection error rate under  $10^{-4}$ . For an inter ion separation of  $5.04\ \mu\text{m}$ , single addressing is successfully achieved with a crosstalk error of  $\sim 10^{-3}$ .

## Table of Contents

1. Introduction .....	6
2. Background .....	8
Motivation: Quantum information processing (QIP) and Quantum error correction (QEC) .....	8
Literature Review: State detection in ion traps .....	10
Literature Review: Individual addressing in ion traps.....	12
3. Experimental Apparatus .....	14
The $^{88}\text{Sr}^+$ ion as a qubit .....	14
The ion trap .....	16
Vacuum chamber.....	18
Lasers.....	18
Ionization lasers.....	19
Repump lasers .....	19
Detection, cooling and pumping 422 nm laser .....	19
Narrow linewidth 674 nm laser .....	19
4. The imaging and individual addressing module.....	21
Optical layout .....	21
The objective .....	22
The acousto-optic deflectors.....	23
The PMT.....	25
The Camera .....	25
Mechanical layout .....	26
Objective Holder .....	28
Optical table and camera holder .....	28
5. Detection .....	30
PMT Detection .....	30
PMT detection of bright and dark states.....	30
Camera Detection .....	33
Determining imaging magnification.....	33
Imaging point spread function.....	33
Camera detection of "bright" and "dark" states .....	34
Multi-ion detection .....	37
6. Individual Ion Addressing .....	39
Individually addressed Rabi oscillations .....	39
Spatial control of individual addressing beam .....	40
7. Summary and outlook.....	43

Outlook..... 43

## Introduction

Quantum mechanics presents us with a picture of nature that is often construed as counter intuitive. However, it is also a picture that has brought about an unparalleled ability to precisely predict and control physical systems, to the point where its validity is widely agreed upon by the scientific community. In order to further understand and utilize the strange or counter-intuitive behavior of quantum mechanics one must be able to perform experiments on such systems in a way that preserves their quantum properties. These sorts of experiments are challenging on two counts: firstly, more often than not, fundamental quantum behaviors are exhibited most blatantly in microscopic systems; secondly, these quantum mechanical phenomena are extremely delicate, and are lost with minimal interaction with the external environment or noisy experimental procedure due to a process known as *decoherence*. Hence, an ideal system to probe quantum mechanics would need to provide a high degree of isolation from the environment, a high degree of control, and an object of study in which quantum mechanical traits are manifest.

One of the prime options for such an endeavor is an array of ions in a Paul trap, in which these ions are suspended in space by quickly alternating electric fields. The ion is an inherently quantum mechanical creature, as its internal state is discrete due to the nature of the electron orbitals and the spin of both the electron and the nucleus. By constructing a Paul trap in ultra-high vacuum and shielding it from unwanted electromagnetic fields, one has an apparatus that can localize a quantum system to a small volume while effectively decoupling it from most environmental interactions. Furthermore, one can manipulate the internal and motional state of the ion in the trap using electromagnetic fields in both the optical, RF and microwaves regimes. Finally, using laser techniques such as Doppler and resolved sideband cooling, it is possible to cool the ion to its motional ground state, allowing for an even higher degree of control.

A major avenue of research for highly controlled quantum systems in general and Paul traps in particular is quantum information processing (QIP). It has been shown that utilizing the superposition properties of quantum systems allows us to efficiently perform computational tasks that are intractable with classical computers, with a notable example being Peter Shor's algorithm for factorization of large numbers in polynomial time. It turns out that such systems are also convenient for researching many quantum mechanical phenomena, and in particular simulating quantum mechanical traits of many body systems and molecular interactions. In a typical QIP scenario, a register of  $N$  two-level quantum states, or qubits, is prepared in a chosen state of the  $2^N$  dimensional Hilbert space and then

acted upon by a series of logical gates amounting to some computational task; the state of the register is then read out, giving the computation result. In Paul traps, these quantum processors can be realized by using each ion as a qubit, and by performing preparation, gates and readout with EM fields.

In order to carry out a general QIP task, one must have the ability to enact a set of logical gates that can be concatenated to perform any possible rotation in the  $2^N$  dimensional Hilbert space. The ability to selectively address any single qubit in the register is an essential feature for this feat. Furthermore, one must have the ability to read out the state of the quantum register with no ambivalence, such that each state is uniquely identified. In Paul traps, both of these requirements pose a technical challenge. The ions, representing the qubits, are typically only a few micrometers apart; since readout is almost invariably done by detecting fluorescence from the ion, a scheme is needed in order to differentiate the fluorescence source with micrometer sensitivity. An additional difficulty is that the readout must be performed quickly so as to allow for many such iterations within the coherence lifetime of the ion; this in turn limits the time to collect fluorescence emission. Similarly, selective addressing imposes the requirement to differentiate in some manner the ion being addressed from its peers, and to be able to do so for every single ion.

The following thesis will outline the construction and testing of an individual addressing and simultaneous many-qubit readout module for an existing Paul trap of  $^{88}\text{Sr}^+$  ions. Prior to the construction of this module, laser manipulation of the ions was performed using a global laser beam, or with a micromotion-based single addressing scheme, efficiently applicable to only two ions; readout was done with a PMT, giving rise to ambivalence as to which ions are the ones fluorescing. The module solves these problems by introducing a fast and highly efficient EMCCD camera which utilizes spatial separation for unique state detection, and by adding a tightly focused laser beam steered by two acousto-optic deflectors for fast selective individual addressing.

## Background

### Motivation: Quantum information processing (QIP) and Quantum error correction (QEC)

The idea of harnessing quantum mechanics in order to perform computational tasks that are difficult or intractable on classical computers was first conceived by several scientists in the early 1980's. Notably, in 1982, Richard Feynman suggested that the computational hurdle of simulating the exponentially growing degrees of freedom of a quantum many-body system could be alleviated by using a similar quantum system in order to perform the simulation (Feynman 1982). In 1985 David Deutsch theoretically described a universal quantum computer through a quantum Turing machine (Deutsch 1985). In a 1992 paper Deutsch, along with Richard Josza, detailed the Deutsch-Josza algorithm for solving a computational problem with a quantum computer exponentially faster than any classical deterministic algorithm (Deutsch 1992). In 1994, however, Peter Shor provided the first proof of the real benefits of quantum computers by detailing Shor's algorithm for integer factorization, a polynomial-time algorithm as compared to the sub-exponential-time classical alternative (Shor 1994).

In 1996 David DiVincenzo succinctly listed a set of criteria a physical system would need to meet in order to perform as a quantum computer (DiVincenzo 1996), which were revised in 2000 (DiVincenzo 2000): i. The system should have a precisely delineated Hilbert space upon which the computation takes place, preferably decomposable to a direct product form (i.e. well defined qubits); ii. The system can be initialized to a fiducial state; iii. The system should be highly isolated from the environment, i.e. long coherence times compared to operation time; iv. The system can be selectively acted upon by a set of universal quantum gates; v. A (strong) measurement scheme is needed.

One of the physical systems that fulfill all these requirements is an ion array in an ion trap. A qubit can be encoded on any two electronic levels of the ion; the system can be optically pumped to a fiducial state; ions in a trap have long coherence times; and the quantum states of the ions can be measured by laser fluorescence. A conceptually non-trivial criterion for ion trap architectures is (iv.), realizing a set of universal quantum gates. This is a set which allows one to approximate any unitary operation on the computational Hilbert space by a finite sequence of set gates; common sets include single-qubit operations and two-qubit entangling gates. In 1995, Ignacio Cirac and Peter Zoller formulated a way to use the

motional modes of ions in an ion trap as a means to entangle two ions (Cirac and Zoller, 1995), and later that year the Ion Storage Group at NIST experimentally demonstrated a CNOT (controlled-not) gate entangling ions (Monroe et al., 1995), thereby paving the way for ion trap quantum computing. Since then, several logical gates, quantum algorithms, quantum error correcting codes and multi-particle entanglement have been demonstrated with ion traps.

Complete isolation of a physical system from the environment is exceedingly difficult. Since quantum coherence is both very delicate and crucial for quantum computation to work, a way to work around or with errors induced by environment or imperfect experimental apparatus is vital. Happily, quantum error correction (QEC) is possible and has been shown to enable fault-tolerant quantum computation for arbitrarily long computations given a suitably low error rate; the error threshold is often taken to be  $\sim 10^{-4}$  for a single gate operation. Classical error correction protects information by redundantly cloning it. However, the quantum mechanical no-cloning theorem states that one cannot clone an unknown state, while the nature of quantum measurement denies the possibility of measuring a state without compromising information, rendering classical methods useless. Nevertheless, it turns out that one can protect quantum information by encoding it on entangled states. In QEC, one encodes the information onto the subspace of larger Hilbert Space. In case of error, it is possible to perform a "smart" measurement that projects the system onto either the correct subspace - in which case the error is corrected - or an orthogonal subspace, without probing the encoded information. Hence the error is rendered discrete. In case of an orthogonal subspace projection, the measurement outputs an error syndrome which can be used to correct the error, all the while providing no knowledge of the encoded information.

Quantum error correction requires not only the ability to selectively manipulate the qubits via universal quantum gates, but also the means to perform measurements in a way that does not collapse the entire wavefunction of the system; i.e. subspace or qubit-specific measurements. Together with DiVincenzo criteria (iv), it implies that to build a quantum computer one must have the ability to selectively address and measure every single qubit. For ion traps, as a result of the inter-ion proximity, this requirement is a technological challenge; during the past two decades a significant amount of experimental effort has been dedicated to advancing various solutions. The following sections will review the difficulties and the proposed and demonstrated solutions for both the detection and addressing challenges in ion traps.

## Literature Review: State detection in ion traps

State detection in ion traps is almost invariably done by fluorescence emission from the ions. The qubit states are encoded onto some electronic levels of the ion, separated by optical, microwave or radio frequencies. In order to differentiate between the  $|0\rangle$  and  $|1\rangle$  states, a state-selective fluorescence scheme is used: upon illumination by a laser at the resonance wavelength, population of (e.g.) the  $|0\rangle$  state will cause the ion to fluoresce, while population of the  $|1\rangle$  state will not. While the qubit can be encoded in various ways on the same ion, at the time of the measurement the qubit must be translated to a basis in which state-selective fluorescence is possible. Transferring the electron population to the non-fluorescing state is termed "electron shelving". The fluorescence can then be detected by any photon detecting device; commonly photo-multiplying tubes (PMTs) and charge-coupled device (CCD) cameras are used for this purpose. The electron shelving technique for state detection was first suggested by Dehmelt (1975) and demonstrated by several groups a decade later (Nagourney 1986) (Sauter 1986) (Bergquist 1986).

Naively, detection fidelity is determined by the degree of separation of the Poissonian distributions of photon counts for the "bright" and "dark" scenarios. On the one hand, this separation decreases when exposure time is reduced; conversely, when increasing exposure time the finite lifetime of the electronic state onto which the electron population is shelved enters play and reduces fidelity. Hence an optimal point can be reached for detection, usually on the order of 1 *ms*. Several groups report high fidelity measurement of a single ion state within the threshold for fault-tolerant quantum computation. (Myerson et al, 2008) use a time dimension maximum likelihood method, based on time of arrival of photons, in order to achieve a fidelity as high as 99.99% in 145  $\mu s$ . (Hume et al, 2007) use an ancilla qubit to reach a fidelity of 99.94%. (Keselman et al, 2011) make use of a narrow-linewidth laser to demonstrate detection fidelity of 99.89% on a Zeeman qubit. (Burrell et al, 2010) achieve 99.99% fidelity for simultaneous readout of several qubits.

Differentiable qubit state detection is crucial for quantum algorithms and quantum error correction. While PMTs allow for fast readout times and provide exceptionally low inherent noise, they lack the spatial differentiation provided by CCD cameras. When used to measure total fluorescence from an ion chain, a standard PMT cannot, for example, distinguish a  $|10\rangle$  state from a  $|01\rangle$  state, as they both emit the same number of photons. Besides cameras, the most popular solution to this problem is individual ion shuttling. (Rowe et al, 2002) report shuttling a single ion between two traps separated 1.2 *mm* apart in 50  $\mu s$

time, with negligible motional heating and while maintaining electronic coherence. Furthermore, they demonstrate a separation of two ions - transferring one of the ions to a different trap - albeit with 10 *ms* time, 95% success rate and a heating of 150 quanta. (Barrett et al, 2004) report an improvement on the same trap, with no detectable failure rate and significantly reduced heating, during a separation time of a few hundred  $\mu s$ . (Hensinger et al, 2006) report shuttling ions two-dimensionally across corners in a T-junction trap architecture, also with 10 *ms* time and 58% success rate. One should mention that shuttling ions can provide a solution not only for differentiating ions in a PMT measurement, but also for qubit-specific detection and addressing. This method was useful in demonstrating quantum algorithms (Chiaverini et al, 2005) and error correction (Chiaverini et al, 2004), and work on improved segmented trap architecture for more efficient shuttling is continuing.

Detection by CCD cameras, on the other hand, avoids the problems of differentiation altogether. Ions are typically separated by distances of 2 – 10  $\mu m$  and fluoresce at order 0.5  $\mu m$  wavelengths; meaning that an imaging system with high enough numerical aperture can image the ions on a camera in a resolved fashion. (Acton et al, 2006) use a CCD camera to perform single qubit detection with 99.4% fidelity and simultaneous detection of multiple qubits with 98% fidelity on a 15 ms readout time, with most of the error due to detection cross-talk. (Burrell et al, 2010) significantly improve on this result with about 99.99% fidelity on both a single ion and multiple ions, at a 400  $\mu s$  detection time. In order to augment fidelity and reduce crosstalk error, Burrell et al. implement a maximum likelihood method that takes into account the probability distribution for bright and dark exposures for each pixel, utilizing the spatial resolution of the imaging system.

As mentioned earlier, for quantum error correction one would need to be able to measure only part of the qubit register. In order to perform such a measurement, ions must be either separated spatially or otherwise decoupled from the measuring scheme. Both of these methods have been implemented. (Barrett et al, 2004) use the shuttling method to demonstrate quantum teleportation. Alternatively, (Roos et al 2004) use a tightly focused laser beam in order to shelve the population of the qubit which is not to be measured into two states which are uncoupled to the fluorescence beam, and with it show the effects of measurement on entangled states.

## Literature Review: Individual addressing in ion traps

As the ions in a Paul trap are typically separated by no more than a few micrometers, and since fault-tolerant quantum computation requires fidelities on the order of 99.99%, individually addressing ions in a chain and maintaining low enough cross-talk to their neighbors is demanding. Logical gate times increase with the ion spacing, preventing the possibility of spreading out the trap. Besides the possible solution of ion shuttling - covered above - there are two central approaches to remedy this difficulty. One method is using a tightly focused addressing beam at the frequency of the optical qubit transition, and precisely controlling its position with an acousto-optic modulator (AOM), electro-optic modulator (EOM) or a micro-electro-mechanical system of mirrors (MEMS). This was first demonstrated by (Nagerl et al, 1999) with an AOM, achieving a beam waist of  $5.7 \mu\text{m}$  Gaussian width. (Crain et al, 2014) use a MEMS-steered system in order to steer a  $3.3 \mu\text{m}$  beam between ions in  $1.1 \mu\text{s}$ . (Hempel, 2014) achieves a focus of  $1.7 \mu\text{m}$  FWHM of the intensity, and improves the cross talk level by replacing the common simple addressing pulse with a composite pulse scheme. This scheme utilizes the fact that while Rabi frequencies are proportional to  $|E|$  - the laser field amplitude - far detuned AC Stark shifts are proportional to  $E^2$ , the laser field intensity, which drops off significantly faster. (Merrill et al, 2014) provide a Lie-algebraic generalization of the composite pulse idea in order to generate a narrowband addressing profile from a broadband beam. Tightly focused addressing beams are also used in neutral atom QIP schemes (Scheunemann et al, 2000) (Weitenberg et al, 2011) (Knoernschild, 2010).

Another approach is differentiating qubit frequencies by inducing a gradient of some external field across the trap. (Staanum and Drewsen, 2002) theoretically propose a single addressing scheme utilizing an off-center detuned laser beam with a medium-sized waist. This laser beam induces a differential AC Stark shift between ions, thereby separating them in frequency space and allowing for single addressing and two-qubit gates without the stringent requirement of tightly focused beams. (Haljan et al, 2005) experimentally realize the AC Stark gradient scheme by encoding qubits on microwave-frequency transitions and shining an off-center  $10 \mu\text{m}$  waist detuned laser beam. An alternate possibility is taking advantage of the RF micromotion present in a Paul trap. A charged particle cannot be trapped by static fields, and thus any architecture to trap an ion in a stationary position must include dynamic fields. In Paul traps these dynamic fields are in the RF regime and account for trapping in the radial direction (as opposed to the trap axis). The motion they induce on the ion is termed micromotion. Although micromotion is often treated as an obstacle, it has been used for individual addressing. (Leibfried, 1998) first proposed using the micromotion in this manner;

(Turchette et al, 1998) and (Navon et al, 2013) implement micromotion induced single addressing effectively.

An alternative is spectrally resolving the ions by a static magnetic fields gradient across the trap, and thus creating a differential Zeeman shift; a scheme first proposed by (Mintert and Wunderlich, 2001). It has been implemented by (Wang et al, 2009) in a surface electrode ion trap, achieving 2.2% crosstalk error between ions separated by  $5 \mu m$ ; and by (Johanning et al, 2009) with 0.4% unwanted excitation of neighbor ions. Recently, (Piltz et al., 2014) used this scheme to demonstrate single addressing on an eight ion chain with a  $10^{-5}$  nearest-neighbor cross talk. A variation on this method is using microwave frequency magnetic fields in a near field configuration as done by (Warring et al, 2013). In their paper, they propose and demonstrate four diverse methods to induce individual addressing with the near field microwave configuration, achieving cross talk errors on the order of  $10^{-3}$ .

## Experimental Apparatus

This chapter presents a short description of the ion trapping experimental apparatus into which the single addressing and imaging module was integrated. It will include three main subchapters: the structure of the  $^{88}\text{Sr}^+$  ion and its use as a qubit; the linear Paul trap; and the laser systems. Further information can be found in (Akerman et al., 2012)

### The $^{88}\text{Sr}^+$ ion as a qubit

Strontium is an alkaline earth metal, and thus when stripped of an electron remains with a single valence-band electron. Consequently, the Strontium cation has a hydrogen-like level structure, albeit with the crucial addition of low-lying meta-stable states in the  $D$  orbital: the  $4D_{\frac{5}{2}}$  (0.38 second lifetime) and  $4D_{\frac{3}{2}}$  (0.44 second lifetime) states. The ground state is given by the  $5S_{\frac{1}{2}}$  state, which can be Zeeman-split into the two different spin states with a susceptibility of  $2.8 \frac{\text{MHz}}{\text{Gauss}}$ . Besides the meta-stable states, the lowest excited state is the  $5P_{\frac{1}{2}}$  state, which is dipole coupled to the ground state allowing for a short lifetime of  $\sim 8$  nanoseconds. The ground state can be coupled to the  $4D_{\frac{5}{2}}$  and  $5P_{\frac{1}{2}}$  states via the electric quadrupole and electric dipole transitions at 674 nanometers and 422 nanometers wavelengths, respectively.

This Zeeman split spin manifold in the ground state is one of the ways in which a qubit can be encoded onto the ion, and transitions between these two states can be driven via an RF field at the transition frequency. Alternatively, the qubit can be encoded on any chosen pair levels of the states in the  $5S_{\frac{1}{2}}$  and  $4D_{\frac{5}{2}}$  levels, separated by the electric quadrupole optical transition. This optical transition is driven via the 674 nm laser.

Preparation of the qubit in a chosen Zeeman state is done by optical pumping, either with the 674 nm or 422 nm lasers. In the first case, the narrow 674 nm quadrupole transition is utilized to selectively excite the population of one of the Zeeman states to the  $4D_{\frac{5}{2}}$  state, and from there the population is pumped to the  $5P_{\frac{3}{2}}$  state by a 1033 nm laser. The population then spontaneously decays to both Zeeman  $5S_{\frac{1}{2}}$  levels. Finally, the ion will end up in the spin state which is uncoupled from this cycle (dark state). In the latter case, the polarization of the 422 nm laser is chosen to be circular such that only one of the Zeeman levels can be excited to the  $5P_{\frac{1}{2}}$  state, from which it can spontaneously decay. The ion will end up dark spin

state which is uncoupled from this fluorescence cycle due to angular momentum conservation.

Detection is done by state-selective fluorescence, with 422 nm laser scattered off the ion from the  $5S_{\frac{1}{2}} \leftrightarrow 5P_{\frac{1}{2}}$  transition. Consider the optical qubit  $5S_{\frac{1}{2}} \leftrightarrow 4D_{\frac{5}{2}}$ : if the qubit collapses to the  $5S_{\frac{1}{2}}$  state, the ion fluoresces via the  $5S_{\frac{1}{2}} \leftrightarrow 5P_{\frac{1}{2}}$  transition and the emitted photons can be detected. If, on the other hand, the qubit collapses to the  $4D_{\frac{5}{2}}$  state, the  $5S_{\frac{1}{2}} \leftrightarrow 5P_{\frac{1}{2}}$  transition is not driven and the ion emits no photons. Since the detection time can be many orders of magnitude shorter than the  $4D_{\frac{5}{2}}$  lifetime, spontaneous decay to the ground state has a negligible effect on detection fidelity. When using the Zeeman qubit, the qubit state can be mapped onto the optical qubit by selectively moving one of the Zeeman states to the  $4D_{\frac{5}{2}}$  state with the 674 nm laser. The detection then proceeds as with the optical qubit.

In order to support the procedures above, two "repump" lasers are needed: the 1092 laser corresponding to the  $4D_{\frac{3}{2}} \leftrightarrow 5P_{\frac{1}{2}}$  transition, and the 1033 laser corresponding to the  $4D_{\frac{5}{2}} \leftrightarrow 5P_{\frac{3}{2}}$  transition. The first is required in order to maintain fluorescence from the ion. When collecting fluorescence, the ion is excited from the  $5S_{\frac{1}{2}}$  to the  $5P_{\frac{1}{2}}$  state, and then spontaneously decays back to the  $5S_{\frac{1}{2}}$  state while emitting a photon. However, there is also a  $\frac{1}{15}$  probability to decay to the  $4D_{\frac{3}{2}}$  state, which due to its long lifetime brings the fluorescence cycle to a halt. The repump 1092 nm laser, when properly tuned, re-excites the ion to the  $5P_{\frac{1}{2}}$  state and allows for continued fluorescence emission. The 1033 laser is used to clear the ion from a  $4D_{\frac{5}{2}}$  population, usually once a detection cycle is done and one wishes to re-initialize the ion in the ground state without waiting for spontaneous decay from the long-lived  $4D_{\frac{5}{2}}$  state.

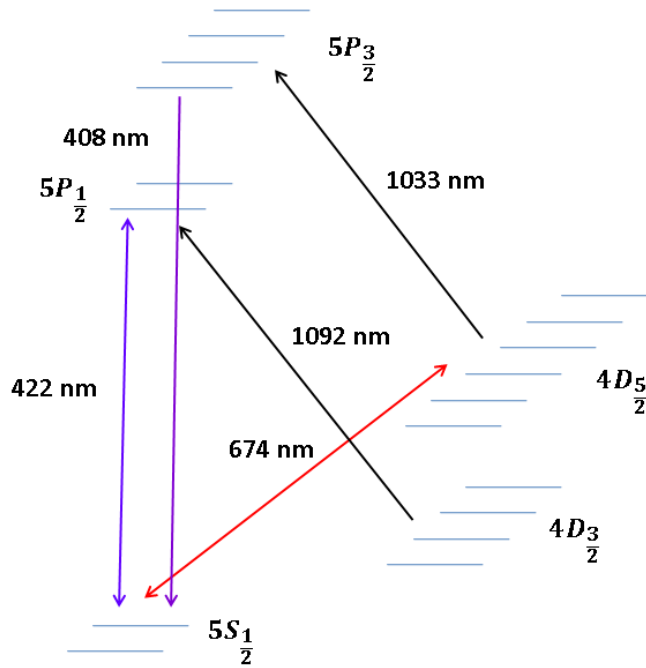


**Figure 3.1 – Energy level scheme for an  $^{88}\text{Sr}^+$  ion.** The ground state is the  $5S_{1/2}$  state, which is split into 2 Zeeman sublevels. The fluorescence and cooling transition is the dipole-allowed  $5S_{1/2} \leftrightarrow 5P_{1/2}$  separated by **422 nm**. **1092 nm** repump is needed to prevent spontaneous decay into the  $4D_{3/2}$  state. Optical qubit is encoded onto quadrupole-allowed **674 nm**  $5S_{1/2} \leftrightarrow 4D_{5/2}$  transition.  $4D_{5/2}$  and  $4D_{3/2}$  are long lived ( $\sim 0.4$  sec lifetime).

## The ion trap

The ion trap is a linear Paul trap. Four parallel conducting cylindrical tungsten electrodes, 0.3 mm in diameter, are placed in a quadrupole configuration, their centers placed on the corners of 0.6 mm square. In the center of this square, another two tungsten rods - hereby known as "end-caps" - of 0.2 mm diameter are placed, one at each side of the trap, such that the distance between their ends is 1.3 mm. Of the four outer electrodes, two opposite diagonal electrodes are held at constant voltage while the two others conduct a 21 MHz oscillating voltage, leading to a confinement in the radial direction. The two end caps are also held at constant voltage, providing the axial confinement. Two additional electrodes are placed slightly below the trap: one is used for applying RF fields on the ions, and the other is used as another DC source, in order to change the equilibrium position of the ion.

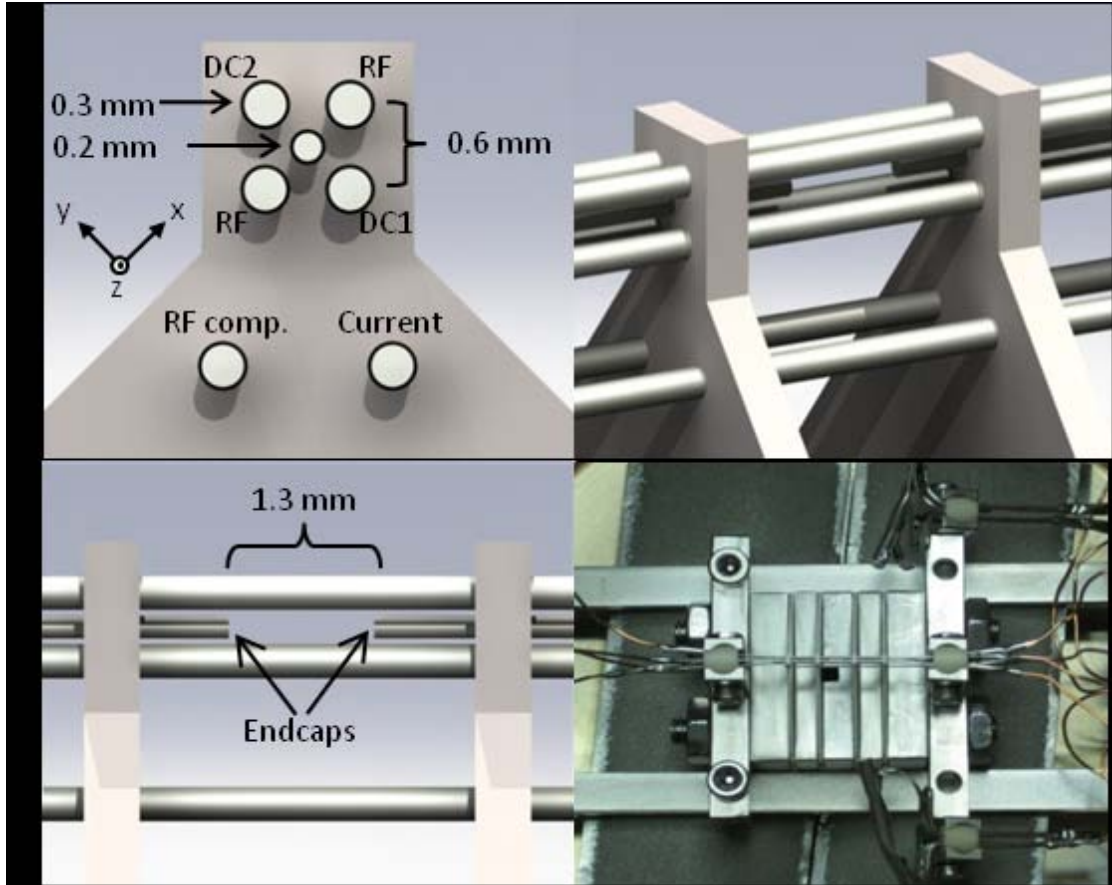


**Figure 3.2 - The Paul trap.** Four parallel cylindrical tungsten rods of  $0.3 \text{ mm}$  diameter are held in a  $0.6 \text{ mm}$  square. On two sides of the trap  $0.2 \text{ mm}$  diameter “endcap” tungsten rods are set along the trap axis, ends separated by  $1.3 \text{ mm}$ . Two additional rods are set  $1.66 \text{ mm}$  below the trap for RF driving and DC compensation along the RF electrodes axis. Images courtesy of Nitzan Ackerman.

The electrodes and end-caps together create a nearly harmonic pseudo-potential leading to typical confinement frequencies of  $\sim 2 \text{ MHz}$  in the radial directions and  $\sim 1 \text{ MHz}$  in the axial direction. The lower axial frequency causes the 1D crystal of trapped ions to align in the axial direction. The interplay between the trap confinement and the natural Coulomb repulsion between the ions determines the spread of the ion chain in the trap and the inter-ion distances. While the distance between ions changes as a function of their number and position in the chain, a typical length scale  $l$  for inter ion distance can be determined by (James,1997)

$$(3.1) \quad l = \sqrt[3]{\frac{Z^2 e^2}{4\pi\epsilon_0 M \nu^2}}$$

Where  $Z$  is the degree of ionization,  $e$  the electron charge,  $\epsilon_0$  the vacuum permittivity,  $M$  the ion mass and  $\nu$  the trap axial frequency. For our trap, with a typical  $\nu = 1 \text{ MHz}$ , we get

$$l = 3.464 \times 10^{-6} \text{ m.}$$

For a small number of ions, the chain size end-to-end is roughly  $l \times 4.569(N^{0.353} - 1)$ , while the closest neighboring ions are in the middle of the chain with an approximate distance of  $l \times \frac{2.018}{N^{0.559}}$ .

### Vacuum chamber

The Paul trap is mounted inside a vacuum chamber maintaining Ultra High Vacuum of about  $10^{-11}$  Torr. The vacuum environment is crucial for preventing collisions of arbitrary particles with the ion chain. Besides heating, these collisions can cause chemical reactions of the Strontium ions with the background gas and thus lead to loss of ions from the trap or a change in their chemical identity. The vacuum chamber is octagonal shaped, with windows in five of the eight side facets and a sunk window in the upper facet. Two of the side facets are used for supplying electricity to the trap and one is used for the vacuum pump.

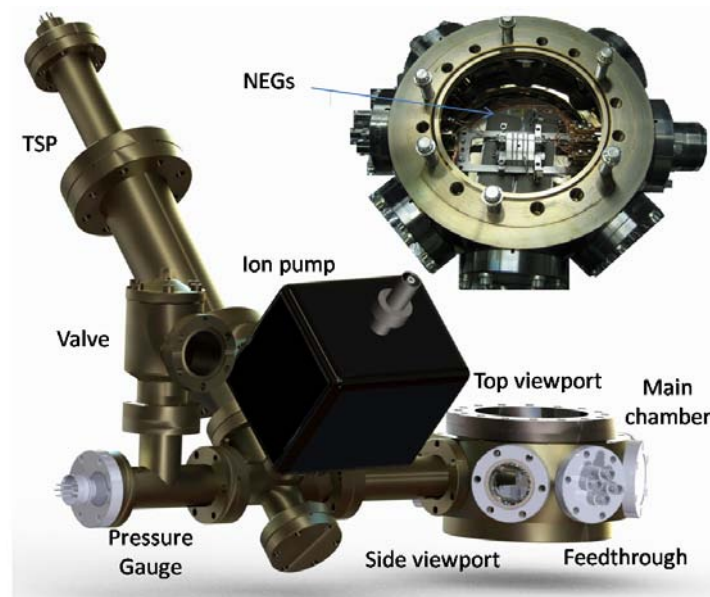


**Figure 3.3 - The vacuum system.** The Paul trap is mounted in the octagon shaped “Main chamber”.

### Lasers

The experiment utilizes 6 different lasers: two lasers for photo-ionization, two "repump" lasers, the 422 nm laser which is used for detection, optical pumping and Doppler cooling, and the 674 nm laser which is used for manipulation of the optical qubit and optical pumping.

### Ionization lasers

The Strontium atoms are photo-ionized by a two-photon process with two independent lasers. First, the atom is excited from the ground state  $5s^2 \ ^1S_0$  to an excited state  $5s5p \ ^1P_1$  by a 461 nm laser, which is generated via a 2<sup>nd</sup> harmonic generation process from a 921 nm ECDL coupled to a nonlinear crystal. The excited state is then further excited to the  $5p^2 \ ^1D_2$  state with a 405 nm laser generated by a diode. The atom then decays into the continuum, leaving an  $^{88}\text{Sr}^+$  ion and a free electron.

### Repump lasers

The 1092 nm  $4D_{3/2} \leftrightarrow 5P_{1/2}$  repump laser is produced by a DFB which is locked to a Fabry-Perot cavity by the Pound-Drever-Hall method. The 1033 nm is produced by an ECDL and is locked to the same cavity.

### Detection, cooling and pumping 422 nm laser

This laser is generated by an 844 nm ECDL coupled to a butterfly cavity with a frequency-doubling BBO nonlinear crystal. The 844 nm emission is locked to an external cavity by a Pound-Drever-Hall method through PZT control of the ECDL grating. The cavity length is then locked by a saturation-absorption method to a Rubidium vapor cell, which provides a frequency 440 MHz detuned from the desired transition in Strontium. Two double-pass AOMs are used to mitigate the difference and generate both a far-detuned (360 MHz) off-resonance cooling beam and a close to resonance beam which is used for detection, optical pumping, and slightly detuned for near-resonance cooling.

### Narrow linewidth 674 nm laser

The 674 nm laser is used for coherent manipulation of the optical qubit, and hence must be narrow enough to selectively address desired Zeeman states and perform coherent manipulation with a minimal error from frequency noise. For this task the 674 laser has four locking mechanisms that bring its linewidth down to  $\sim 120$  Hz at  $\sim 100$  seconds. The laser is first generated by an External Cavity Diode Laser (ECDL) in a Littrow configuration. It is then modulated at 20 MHz by an EOM and locked to a high finesse cavity ( $f = 86000$ ) by the Pound-Drever-Hall method, through a fast modulation of the diode current and slow feedback on the ECDL grating. After this first locking mechanism, the optical power transmitted through the cavity of  $\sim 10 \mu\text{W}$  is used to filter high frequency phase noise. To amplify the optical power, the stabilized light is injected into a slave diode and optically locks its frequency. The light then passes through an AOM and a portion is cut off and taken to a second high-finesse cavity ( $f = 500,000$ ). The error signal from this second cavity is used to modulate the AOM and correct the frequency. Since the second cavity is connected by a 5-

meter length optical fiber to the rest of the setup, a fiber noise cancellation apparatus is then set up to correct for phase noise induced by the fiber.

## The imaging and individual addressing module

The imaging and individual addressing module enhances the capabilities of the already existing  $^{88}\text{Sr}^+$  linear Paul trap experiment in two ways. The first is providing high-fidelity high-speed simultaneous readout of the state of several ions with no ambivalence. To achieve this goal the ions are optically imaged via  $422\text{ nm}$  fluorescence through a 0.34 numerical aperture objective onto a fast electron-multiplying charge-coupled device (EMCCD) camera, with an option to switch to a photo-multiplying tube (PMT). The second is to enable individual qubit addressing with low crosstalk to neighboring ions for small inter-ion distances. This is achieved by passing a narrow linewidth  $674\text{ nm}$  laser commensurate with the "optical qubit"  $5S_{\frac{1}{2}} \leftrightarrow 4D_{\frac{5}{2}}$  transition through two acousto-optic deflectors - for beam steering capability - and focusing the laser with the same 0.34 NA objective onto the ion chain. The following chapter will consist of a review of the technical details of the system as well as the motivation that went into building the system the way it has been built.

### Optical layout

Figure 4.1 schematically presents the optical set up for the imaging and individual addressing module. The trapped  $^{88}\text{Sr}^+$  ion fluoresces at  $422\text{ nm}$  wavelengths emitting  $\sim 10^7$  photons per second. A portion of this emission is collected by a LENS-Optics 0.34 numerical aperture objective with a working distance of  $30\text{ mm}$ , positioned outside the vacuum chamber. The light is then focused directly by the objective onto the Andor iXon Ultra EMCCD camera positioned  $\sim 1250\text{ mm}$  away from the objective, providing a  $\times 40$  magnification. A dichroic long-pass mirror reflects the  $422\text{ nm}$  fluorescence onto the camera while allowing the  $674\text{ nm}$  addressing beam to pass through. A dove prism is set near the camera in order to correct the orientation of the ion chain to that of the pixel rows of the camera, and the camera is fitted with a  $422\text{ nm}$  filter for the purpose of cleaning out unwanted background light. A flipping mirror is set nearby to the camera and can divert the light to a Hamamatsu PMT, also fitted with a  $422\text{ nm}$  filter.

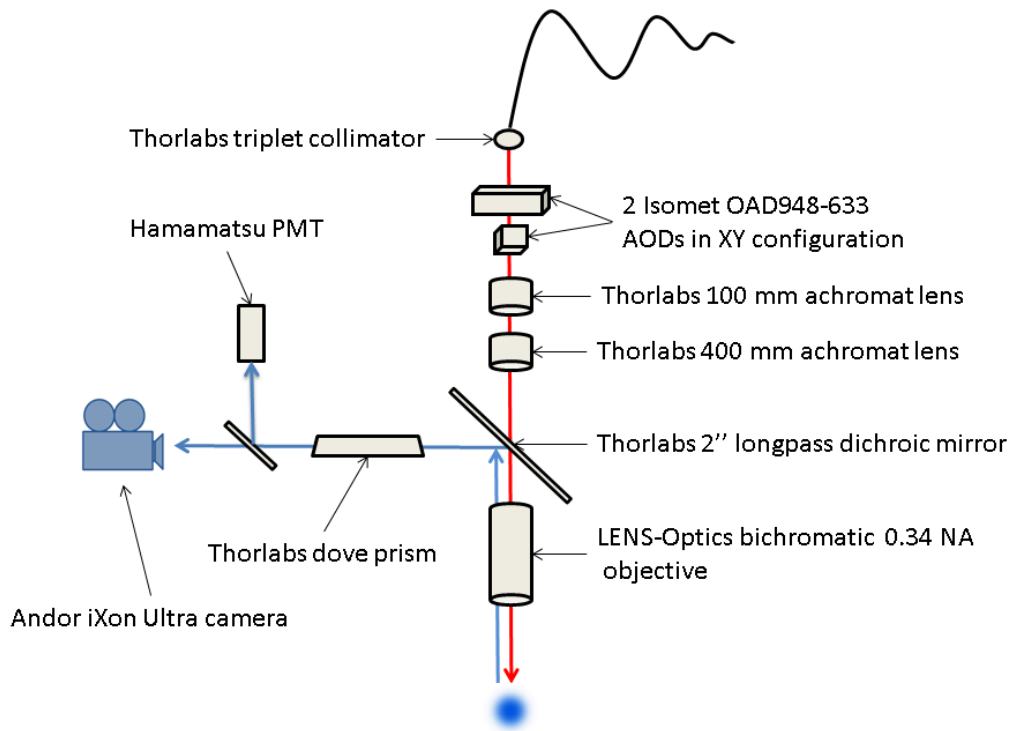


**Figure 4.1 - Optical layout.**  $674 \text{ nm}$  beam shown in red,  $422 \text{ nm}$  fluorescence shown in blue. The addressing beam exits the optical fiber through a triplet collimator into the XY configured AODs. It is then magnified with 2 doublet lenses and passes through a dichroic longpass mirror to the objective and onto the ion. Fluorescence is collected by the objective and focused onto the camera and PMT, reflected by the longpass and rotated with a dove prism.

The narrow linewidth  $674 \text{ nm}$  addressing beam is brought to the system by an optical fiber and collimated by a low-aberration triplet collimator to a  $1.1 \text{ mm}$  waist. The beam then passes through two Isomet OAD948-633 acousto-optic deflectors set in an XY configuration. The deflectors allow for precision control of the beam direction by applying appropriate RF frequency input. The deflected beam passes through a  $100 \text{ mm}$  achromatic lens which creates a focus close to the ion image plane. For an easier control of the beam focus, a  $400 \text{ mm}$  achromatic lens is added a few centimeters after the image plane, slightly translating the effective focus of the expanding beam. Both lenses are achromatic doublets, as such lenses induce fewer aberrations than standard thin lenses. The expanding beam then passes through the dichroic longpass and into the objective, which focuses it on the ion chain.

### The objective

The objective is from LENS-Optics and has a numerical aperture of 0.34 with an effective focal length of  $30 \text{ mm}$ , and is built from 1-inch diameter lenses. Since it must image at  $422 \text{ nm}$  as well as focus at  $674 \text{ nm}$ , it is specifically corrected for chromatic aberrations at

these wavelengths. As the objective is located outside the vacuum chamber, it is separated from the trap by 3.3 mm thick fused silica window; this fact is also taken into account for the purpose of aberration correction. Assuming a working distance equal to the focus of  $f = 30$  mm, the fraction of light collected by the objective is:

$$(4.1) \quad \text{eff}_{obj} = \frac{\pi \left(\frac{D}{2}\right)^2}{4\pi f^2} = \frac{1}{4} \left(\frac{D}{2f}\right)^2 \approx \frac{1}{4} (NA)^2 = 0.0289 \cong 1/35$$

where  $D$  is the objective aperture diameter,  $f$  the objective focal length and  $NA$  the numerical aperture. The objective is designed to work in a  $\infty - f$  configuration, collimating the fluorescence arriving from the ion. However, it became apparent during construction of the system that the objective is in fact faulty and introduces unwanted aberrations, particularly astigmatism. Furthermore, it seemed that adding optical elements after the objective severely aggravates these aberrations. Therefore it was decided that a minimal amount of optical elements will be added to the system, and that the objective would not collimate the ion fluorescence but rather directly image the ions onto the camera. For this reason the objective is positioned slightly farther away from the ions, leading to an estimated photon collection efficiency of  $\sim 1/36$ .

### The acousto-optic deflectors

In order to control the position of the addressing beam on the ion chain with sub micrometer resolution, precise control of the beam angle is needed. Furthermore, in order to be able to carry out a large number of gates within the confines of the coherence time of the qubits, the angular control should allow fast switching between different ions. Lastly, the angular range over which the beam is scanned should be enough to cover a relatively large ion chain. Acousto-optic deflectors are able to satisfy all of these requirements. In an acousto-optic modulator a piezoelectric transducer induces acoustic waves through a transparent medium. The acoustic waves cause periodic variations of the medium's refractive index, and thus light that passes through the material undergoes Bragg diffraction. The angle and frequency of the diffracted beam depend on the PZT frequency, allowing for external control via RF controllers. Acousto-optic deflectors, as opposed to modulators, are built to enable efficient diffraction over a large range of frequencies/angles, making them ideal for spatial control.

The deflection angle- RF frequency relation in an AOD is given by:

$$\Delta\theta = \frac{\lambda}{v} \Delta f$$

Where  $\Delta\theta$  is the change in deflection angle,  $\lambda$  the incident light wavelength,  $\Delta f$  the change in RF frequency and  $v$  is the acoustic velocity of the medium. The resolution  $N$  of the AOD is defined to be the ratio between the total angular range of deflection to the angular width of the beam, which is the total number of resolved spots the deflected beam can scan. A beam of width  $d$  has an angular width of  $\delta = \frac{\lambda}{d}$ , and so

$$N \equiv \frac{\Delta\theta_m}{\delta} = \frac{\Delta\theta_m d}{\lambda} = \frac{d}{v} \Delta f_m \equiv \tau \Delta f_m$$

Defining  $\Delta\theta_m$  to be the total angular span,  $\Delta f_m$  the total frequency span and  $\frac{d}{v} \equiv \tau$  to be the time the acoustic wave takes to cross the beam, which is effectively the time it takes the deflector to change the angle of the diffracted beam.

Our requirements of large deflection range and fast switching times now translates to high  $N$  and low  $\tau$  parameters for the AOD respectively, which are clearly contradicting. Nevertheless, there is a range of parameters for which one can achieve a suitable solution. Since logical gates in the system are usually no shorter than  $1 \mu s$ ,  $\tau$  was chosen to be of that order. Furthermore, since the ion chain in our system is almost never larger than  $50 \mu m$ , and the focused spot size should be on the order of  $1.5 \mu m$ , a resolution of  $50 < N$  was chosen. Both these parameters are achievable with an Isomet OAD948-633 AOD. The OAD948-633 has an acoustic velocity of  $650 m/sec$  and a frequency bandwidth of  $45 MHz$ . Entering the deflector with a beam diameter  $d = 1.1 mm$ , we get

$$\tau = \frac{1.1 \times 10^{-3} m}{650 m/sec} = 1.7 \times 10^{-6} sec; N = 1.7 \times 10^{-6} sec \times 45 \times 10^6 \left( \frac{1}{sec} \right) = 76.5$$

as required.

The beam passes through two identical AODs in an XY configuration, i.e. the AODs deflect in perpendicular axes. This allows controllably reaching every point in a focal plane (as opposed to a line), a property useful for precise positioning of the beam. The two AODs are mounted on an Isomet BA6 mount specifically configured for this XY setup.

## The PMT

The PMT counting head is a Hamamatsu H10682-210. It has a quantum efficiency of 25%, a pulse pair resolution of 20 ns, and a dark count of < 100 photons per second, which translates to under 0.1 photons per typical exposure time of 1 ms.

## The Camera

The camera in use is an Andor iXon Ultra 897 EMCCD. This model is suitable for the detection task due to a high quantum efficiency (> 90%), high sensitivity (single photon sensitivity for some acquisition settings), high readout speeds (a maximum speed of 17 MHz), low temperature thermo-electrically cooling (down to  $-100^{\circ}\text{C}$ , substantially reducing dark current in the CCD array), and high gain (up to  $\times 500$ ). The iXon has  $512 \times 512$  pixels, each pixel  $16 \times 16 \mu\text{m}$  in size. Since the imaging system has a point spread function of  $\sim 1 \mu\text{m}$  diameter (more on that in the following chapter), and a magnification of  $\sim \times 40$ , the ions occupy a 2-3 pixel diameter spot on the iXon CCD. A ten ion chain has a length of  $\sim 20 \mu\text{m}$ , corresponding to  $\sim 800 \mu\text{m}$  or  $\sim 50$  pixels on the CCD.

A short measurement and readout time is desirable for QIP and metrology tasks. The iXon Ultra has two modes that support significant reduction of readout times, which is often a bottleneck in CCD detection architectures: in Frame Transfer mode, the iXon acquires an image onto the image area whilst simultaneously reading out the previous image from a masked frame storage area; Fast Kinetics mode uses the CCD array itself as a storage medium, allowing for a small number of extremely fast exposures. However, neither of these options affords an adequate solution to the desired specification, as in both modes one cannot control the time between exposures. Such a control, through external triggering, is critical to the experiments this module must perform.

In order to sustain minimal readout times while externally triggering the exposures, the camera is worked in Fast External Trigger (FET) mode. In normal External Trigger mode, after completing an exposure, the camera will not accept another external trigger to begin exposure until sufficient cleaning cycles ("External Keep Clean Cycle") of the EMCCD

are complete. The FET mode allows for immediate acceptance of the external triggering at the cost of forgoing the completion of the cleaning procedure, minimizing readout times. Moreover, a small region of interest (ROI) is defined in order to include only the pixels imaging the ion chain; only these pixels are read out, significantly shortening readout time.

The camera is controlled by a PC through a USB connection, and is communicated to through MATLAB via a C++ library of predefined commands for the camera supplied by Andor. By use of this library one can control the camera settings, including acquisition modes, readout modes, temperature, and shutter states. However, since the PC CPU is unsuitable for real time management of experiments, the triggering of detection is done by a field-programmable gate array (FPGA) which controls the rest of the experiment. In a typical experiment the acquisition settings of the camera are set by PC commands, the experimental sequence then starts and the camera acquisition is triggered by the FPGA. At the end of the sequence the data acquired by the camera is read out to the PC through the USB connection. A planned improvement of system capabilities would allow reading the measurements and responding to them in real time, during the course of an experiment.

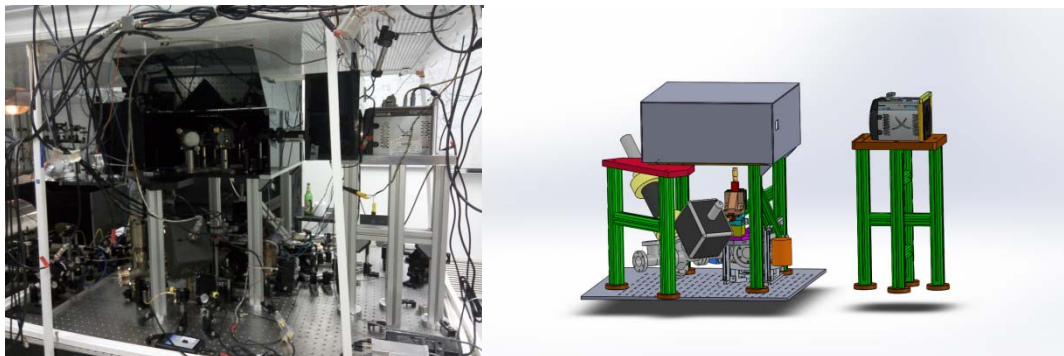


**Figure 4.2 – System mechanical layout.** (Right) a Solidworks model of the mechanical layout and (left) photo of the system. Optical table is fitted with a box in order to minimize stray light noise.

Such an improvement requires implementing readout of the camera through a CameraLink output directly onto a dedicated FPGA, and interfacing this FPGA with the experiment-directing FPGA.

### **Mechanical layout**

The IIA module is constructed from three mechanically separate parts: the objective holder, the optical table and the camera holder. The rationale for this separation is an attempt to quell the effects of mechanical vibrations on the module, and particularly the effects of mechanical vibrations on the positioning of the individual addressing beam. As the individual addressing

beam is tightly focused to a  $\sim 1 \mu\text{m}$  spot on the ion chain, beam pointing vibrations must be constrained to significantly smaller vibration amplitude. Otherwise, the vibration would translate into a time variation of the laser field amplitude on the ion - and consequently a time variation of the addressing Rabi frequency - leading to infidelity of the addressing operations.

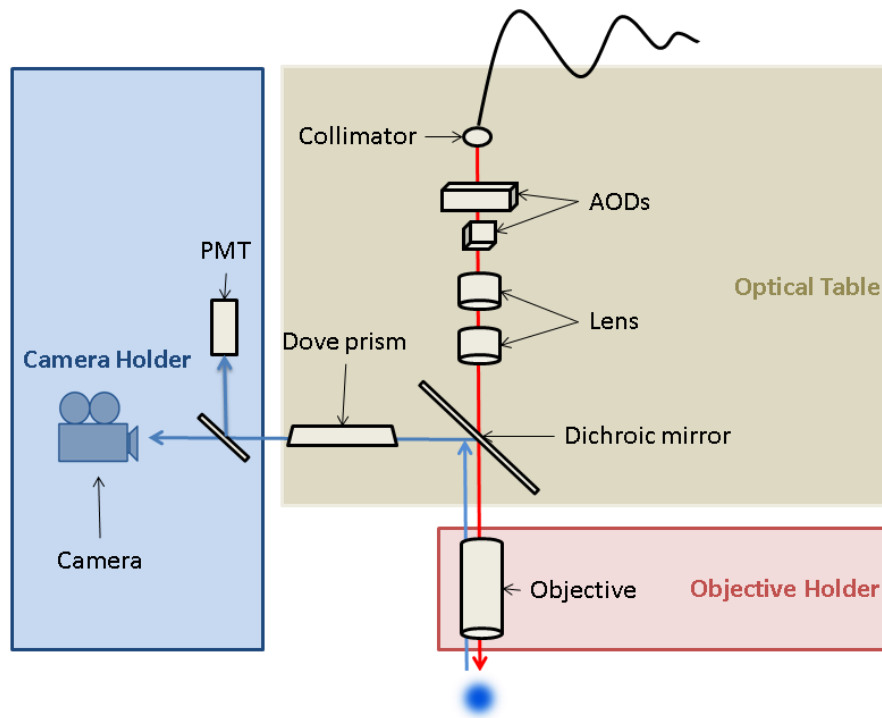


**Figure 4.3 - Optical setup divided by mechanical placements.** The objective holder is connected directly to the vacuum chamber for minimal vibration. Optical table and camera are disconnected in order to suppress vibrations from the camera fan.

The mechanical separation reduces the risks of vibrations in several ways. The Andor iXon Ultra is equipped with a cooling fan; such fans typically produce comparatively large mechanical vibrations. For this reason the camera is set on a separate stage, mechanically decoupled from the rest of the system. The objective holder, containing the objective exclusively, is set directly onto the vacuum chamber. Through strong mechanical connection with the chamber vibrations of the objective with respect to the ions are minimized as much as possible. The rest of the optical system is set on an optical table - a breadboard on 5 supporting legs - which rests directly above the vacuum chamber, decoupled from the two other parts. Although the optical table is liable to harsher vibrations than the objective's, the demagnification of the addressing beam from its first focal point on the optical table to the ions implies that the vibration amplitude is similarly demagnified. Thus, the optical table can withstand vibration amplitudes 40 times more severe than required by the objective.

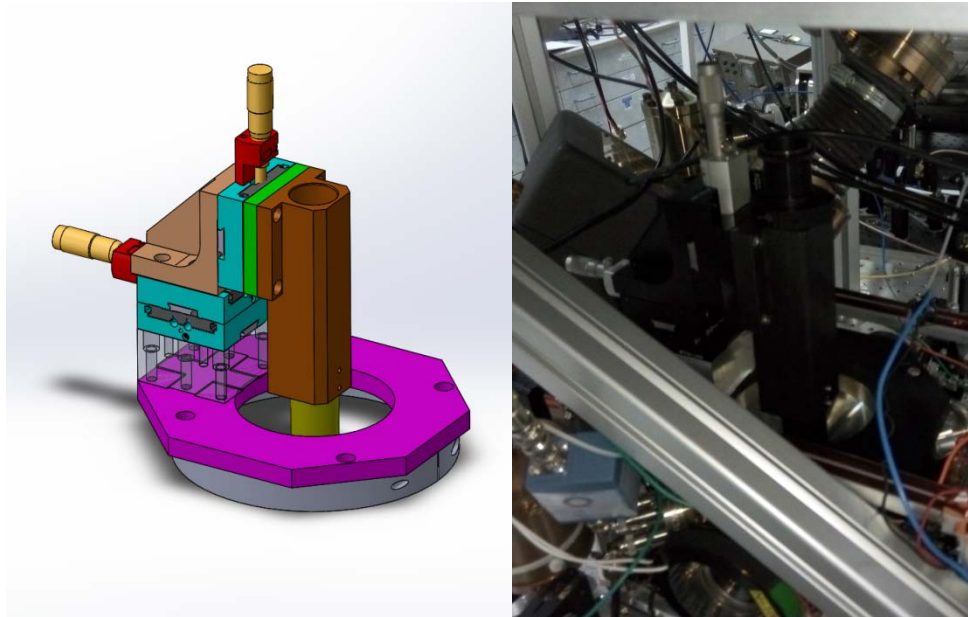


**Figure 4.4 – Objective holder drawing and photo.**

### **Objective Holder**

The objective holder is attached directly to the vacuum chamber. The connection is done by clamping together two half-rings on the exterior of the top protrusion of the chamber. A basis plate is mounted onto the ring, and in turn supports a Newport XYZ translation stage. The stage is mechanically steered through micrometer-resolution actuators in all axes, with a span of 1.1" each. A custom-made stainless steel tube is screwed to the stage and holds the objective. The translation stage allows for positioning the objective above the ion chain and alignment of the focus.

### **Optical table and camera holder**

The top of the optical table is a Thorlabs aluminum breadboard, 1/2" thick, cut to a size of 16" × 19". A 1.5"  $\varnothing$  circular hole is cut through the board to allow addressing and fluorescence light to pass between the objective holder and the table; the hole is placed above the objective and ion trap. There are 5 table legs, placed to avoid contact with the underlying optics and vacuum system. The legs are made of anodized aluminum and have a 40 × 40  $mm^2$  cross section size. Diagonal brace beams are added between legs when possible in order to decrease cantilever-like vibrations of the table, which without braces are common modes to all legs. The optical table itself is fitted with a box to shield stray light from polluting imaging or addressing. The camera is placed on top of a custom made holder designed to rigidly hold the camera in place. The holder is set on a stage with four legs, also

made of anodized aluminum. Not shown in CAD images is a box set on the camera stage, designed to block stray light coming to the camera.

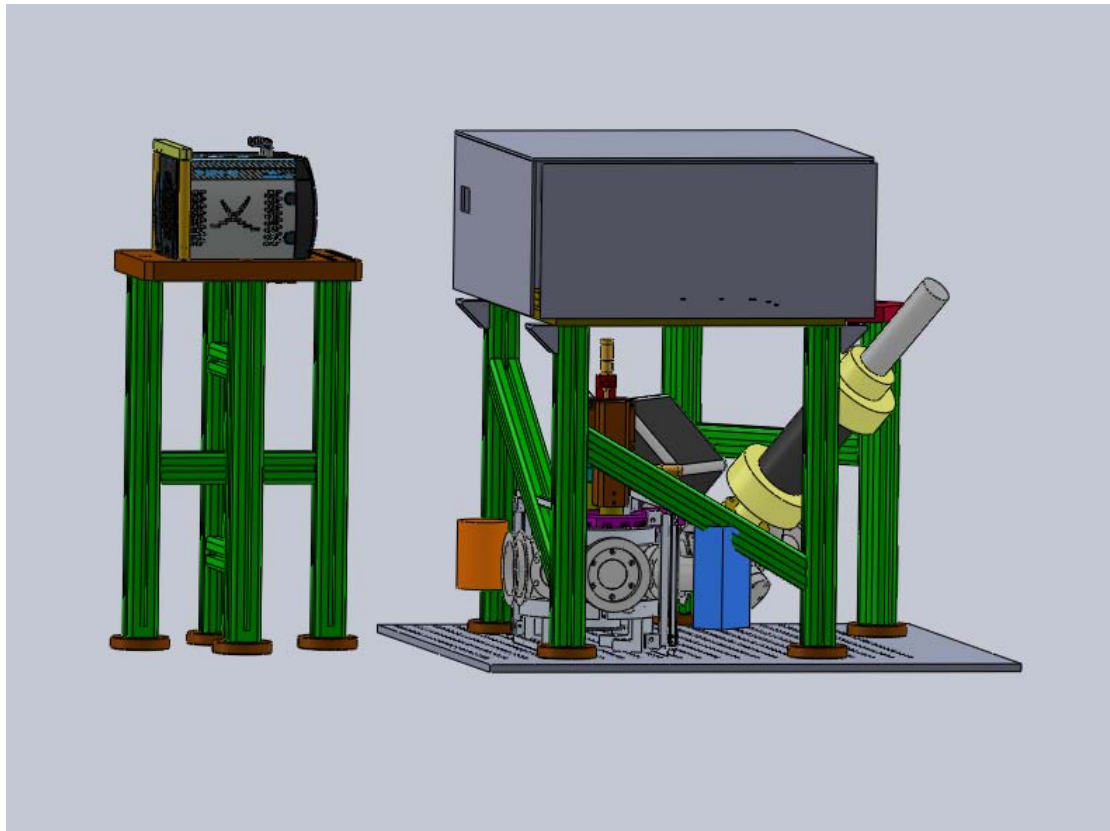


**Figure 4.5 – Another view of the mechanical layout.**

## Detection

This chapter will present and discuss the detection capabilities of the systems with emphasis on the ability of the system to determine the ion state, taken to be "bright" if in the  $5S_{\frac{1}{2}}$  state or "dark" if in the  $4D_{\frac{3}{2}}$  state. There are two options for state detection: either through PMT or through the EMCCD camera. As the PMT is unable to perform unique state detection, for the PMT only single ion state detection will be discussed, while for the camera both single and multi-ion cases are presented.

### PMT Detection

#### PMT detection of bright and dark states

For a single ion, determination of "bright" vs. "dark" state is done by counting the number of photons arriving from the ion at a predetermined window in time, and comparing this number to a threshold number. Since the photon emission process is discrete and random with a fixed probability of emission per unit time, the number of photons detected in a time frame is expected to follow a Poisson distribution with a different mean for each case. A high detection fidelity can then be translated to small overlap of the Poisson distributions for "bright" and "dark" scenarios. Although in a typical experiment the "dark" state is the  $4D_{\frac{5}{2}}$  state, reached by  $674\text{ nm}$  laser shelving, in both the PMT and camera detection measurements we use the  $4D_{\frac{3}{2}}$  state instead. This state is reached with very high fidelity by optical pumping, so measurements of detection fidelity are not constrained by  $674\text{ nm}$  shelving fidelity. The  $4D_{\frac{3}{2}}$  is similar to the  $4D_{\frac{5}{2}}$  in that they are both long-lived and do not fluoresce by  $422\text{ nm}$  laser excitation.

Figure 5.1 shows "bright" and "dark" distribution measurements for a single ion. Each distribution includes  $1.5 \times 10^4$  measurements of  $1\text{ msec}$  time frames. It is evident that although a large number of measurements were taken, the distributions are very well separated. This implies that the detection fidelity ( $= 1 - \text{error rate}$ ) is significantly better than  $1 - 10^{-4}$ . Figure 5.1 also includes a Poisson fit to both distributions, showing they are fairly approximated by a Poisson distribution, as expected.

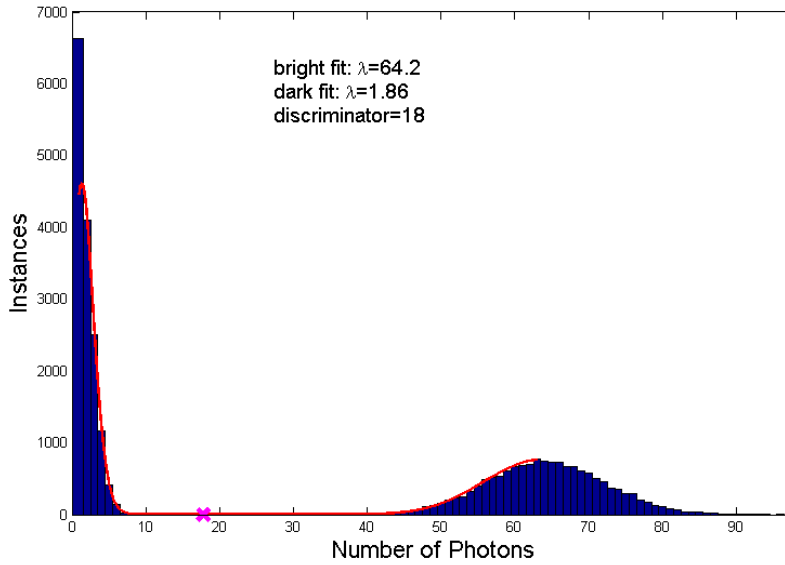


**Figure 5.1 - PMT "bright" and "dark" distribution measurements for a single ion.**  $1.5 \times 10^4$  1 msec measurements taken for each case. "Bright" distribution is shown on the right, and takes the form of a Poisson distribution with mean  $\lambda = 64.2$ . The dark distribution on the left is similarly Poissonian with  $\lambda = 1.86$ . In red is shown a fit to an addition of two Poisson distributions, with the fit minimum indicated by a pink X. This minimum is used as a discrimination threshold, which in this case is 18 photons/1msec.

The undetectable error rate of the given measurement suggests that shorter detection times are feasible, a fact that may be useful when limited coherence times constrain the freedom to use long detection times. The proportion  $\frac{\lambda_{bright}}{\lambda_{dark}}$  should remain approximately invariant to detection time, but the separation of means relative to the distribution widths, i.e. signal-to-noise, is proportional to

$$(5.1) \quad \frac{\lambda_{bright} - \lambda_{dark}}{\sqrt{\lambda_{bright}} + \sqrt{\lambda_{dark}}} = \sqrt{\lambda_{bright}} - \sqrt{\lambda_{dark}},$$

hinting that proportional decrease of both distributions means deteriorating detection fidelity. Indeed this is the case, as shown by Figure 5.2. A detection time of  $200 \mu\text{sec}$  introduces an unacceptable error rate of  $\sim 1 \times 10^{-3}$ , thereby requiring a minimal detection time of  $\sim 400 \mu\text{sec}$ .

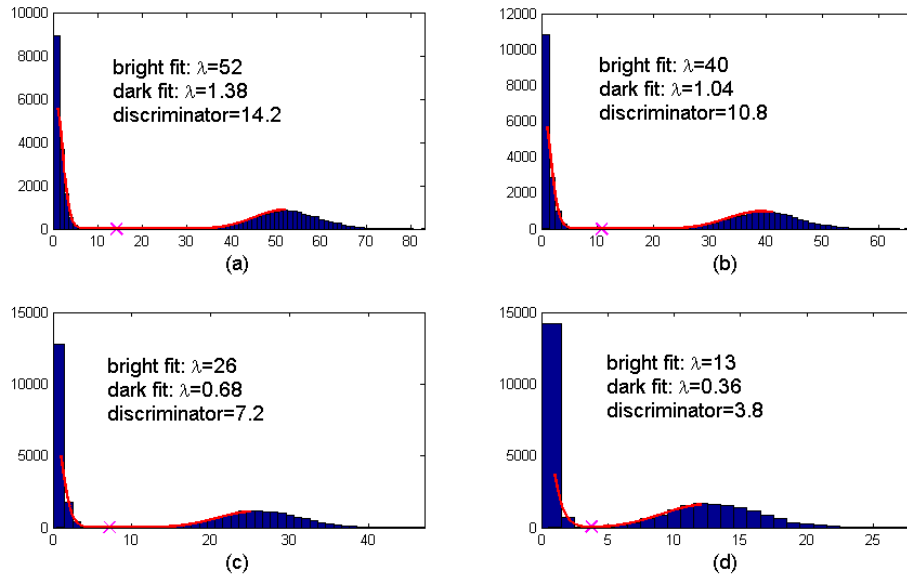


**Figure 5.2 - PMT "bright" and "dark" measurements for different detection times.**  $1.5 \times 10^4$  measurements taken for each case. The different graphs represent detection times of (a) 0.8 msec, (b) 0.6 msec, (c) 0.4 msec and (d) 0.2 msec. All are well separated besides the 0.2 msec scenario, in which 8 false bright and 11 false dark cases were measured out of  $1.5 \times 10^4$ , suggesting an error rate of  $\sim 1 \times 10^{-3}$ , higher than the acceptable rate.

## Camera Detection

### Determining imaging magnification

The magnification of the camera imaging can be determined through the imaged distance between two ions, which can be accurately calculated via the formula given in (James, 1997). For this purpose, a 3 ion image is shown in Figure 5.3, followed by a one dimensional projection of the image onto the ion chain axis. Fitting the projected ion signals to 3 Gaussians, one can determine the distance in pixels between each two ions, which is the distance between ion images on the image plane of the camera. This measured distance can be compared to the actual inter ion distance calculated by (James, 1997), from which one can extract the magnification.

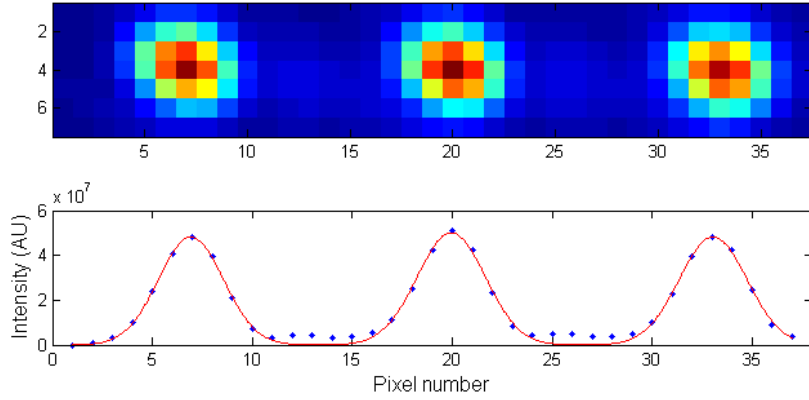


**Figure 5.3- 3 ion image and one dimensional projection and fit.** The top figure is a typical 3 ion image from the Andor iXon Ultra EMCCD camera. The bottom figure includes a y-axis sum of the image, shown in blue, and a fit to the sum of 3 independent one dimensional Gaussians. The x-axes are camera pixel index numbers. From left to right, the Gaussian centers in pixel units are: **6.93(13)**, **19.95(13)**, **33.04(13)**.

The 3-Gaussian fit yields an imaged inter ion distance of 13.06(13) in pixel size units, which translates to 209.0(2.1)  $\mu\text{m}$ , as the pixels are 16  $\mu\text{m}$  across. The trap frequency is 633 KHz, which gives a length scale of  $l = 4.679 \mu\text{m}$ . For 3 ions, the inter-ion distance is calculated to be  $1.077 \times l = 5.039 \mu\text{m}$ . From here one can extract the total magnification:

$$\text{Magnification} = \frac{209.0(2.1) \mu\text{m}}{5.039 \mu\text{m}} = 41.48(42)$$

in good agreement with the design magnification. The correspondence between pixel size and real distance, which comes to 0.386(4)  $\mu\text{m}/\text{pixel}$ .

### Imaging point spread function

The point spread function (PSF) of an imaging system determines the response of this system to point source. Since our trapped ions are localized to a few tens of nanometers they are effectively a point source. The PSF of the IIA module is therefore simply its image of a single

ion. A sample single ion image is presented in Figure 5.4 along with a two dimensional Gaussian fit, with background contributions subtracted. The full width at half maxima (FWHM) of the PSF in the  $x$  and  $y$  dimensions are given by the fit to be 4.01(4) and 3.69(3) pixels, which translate to  $1.55 \mu\text{m}$  and  $1.42 \mu\text{m}$  on the ion chain, respectively. The tails in the top and right directions, as well as the elliptic shape of the ion image, are a result of coma-like aberrations due to imperfect alignment and optical components.

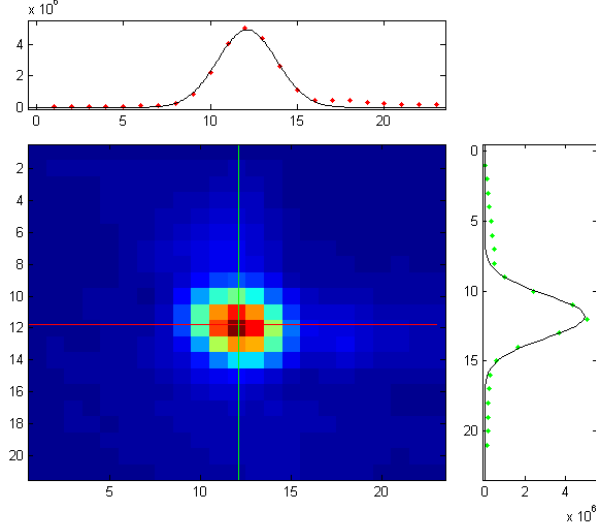


**Figure 5.4 - Single ion image PSF.** In the center is a false-color image of the ion, background subtracted. Above and to the right are fits to Gaussian functions for the  $x$  and  $y$  axes respectively. Gaussian FWHMs are: **4.01(4)**, **3.69(3)** in pixel units or **1.55(2)**, **1.42(1)** micrometers. Aspherical aberrations present in comatic shape of focus and tails.

### Camera detection of "bright" and "dark" states

Camera differentiation of bright and dark measurements (examples shown in Figure 5.5) is done by comparing total intensity over a set of predetermined pixels of interest. In order to do so, a discrimination threshold is set individually for each ion using the following process, illustrated in Figure 5.6: a) A batch of sample "bright" and "dark" images are acquired; b) pixels are ordered from brightest to darkest according to the average of bright images; c) "Bright" and "dark" intensity distributions are compared for  $n$  brightest pixels, where  $n$  ranges from the single brightest pixel up to all image pixels or up to a predetermined maximum number of pixels; d) the optimal  $n$  (number of brightest pixels) for discrimination is chosen by minimal distribution overlap, or - in the case of no distribution overlap - by maximizing distribution mean distance compared to minimum distance, i.e. taking  $B_n$  and  $D_n$  to represent the bright and dark intensity distributions for  $n$  pixels, the optimal  $n = n^*$  is chosen by:

$$(5.2) \quad n^* = \max_n \left( \frac{\overline{B_n} - \overline{D_n}}{\overline{B_n} - \overline{D_n} - (\min(B_n) - \max(D_n))} \right)$$

where  $\overline{B}_n$  and  $\overline{D}_n$  represent the means of the "bright" and "dark" distributions, respectively. The measure in parentheses attempts to quantify the "separation" of the two distributions and thereby predict the optimal pixel set for discrimination given an even larger data sample. A high separation measure implies that the worst cases for both bright and dark states (high photon count for dark and low photon count for bright) are not bad enough to induce discrimination error, and in fact are separated by a wide margin relative to the mean distribution separation. In contrast to PMTs, the distributions are not Poissonian, as they are altered by camera readout noise and dark currents as well as gain. This prevents using a Poissonian fit method reliably, as done with the PMT. The choice of characterizing separation through worst-case scenarios is natural when taking into account apparent deviations from a Poisson distribution in the distribution tails.

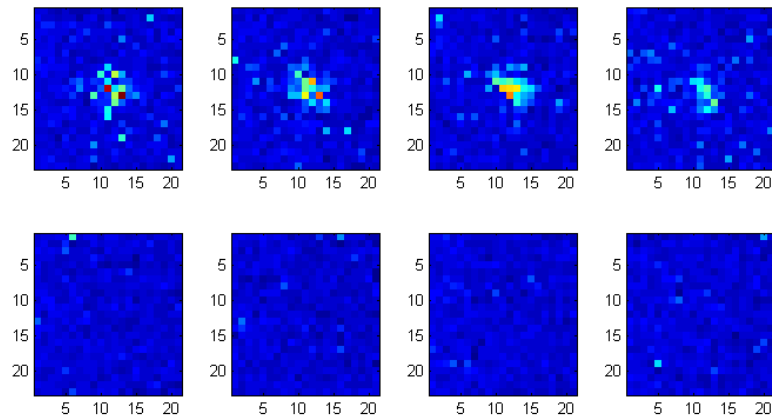


**Figure 5.5 - Sample bright and dark measurements for a 1 msec exposure.** Top row shows bright measurements, bottom row shows dark. For 1 msec exposures the difference is clearly visible, as evidenced by intensity distributions of such measurements shown in Figure 7a.

Adding more pixels compresses the "bright" distribution thereby increasing its separation from the dark distribution. However, as dimmer and dimmer pixels are added, the value of adding new pixels decreases until the separation measure saturates, usually around the 30 – 40 pixel mark. Adding significantly more pixels increases noise and thus deteriorates the separation measure (see Figure 5.6). Similarly to the PMT, the distributions for bright and dark seem to be well separated for this exposure time, indicating an error rate that is significantly smaller than  $1 \times 10^{-4}$ .

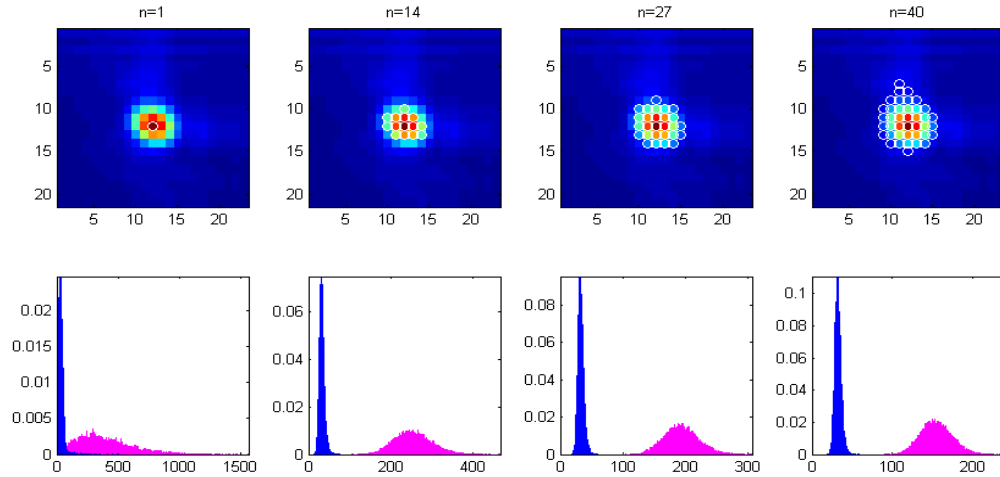


**Figure 5.6 - Camera discrimination setting procedure for a single ion.** The top row presents an image of the ion composed of a sum of  $1.5 \times 10^4$  1 msec "bright" measurements, while the bottom row shows bright (pink) and dark (blue) distributions of the same data set in arbitrary units. In each column, the distributions are taken with respect to the  $n$  brightest pixels only, illustrated in the top row with white circles indicating the relevant pixels.  $n = 1, 14, 27, 40$  are shown for demonstration, although all intermediate possibilities are also considered.

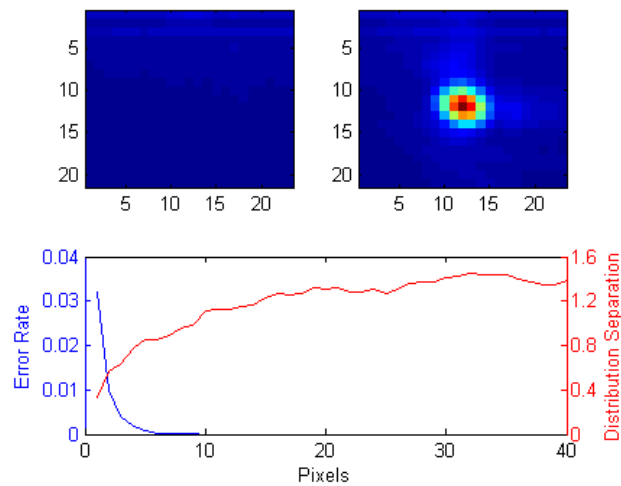


**Figure 5.7 - Camera discrimination setting procedure for a single ion.** Top panel shows summed "dark" (left) and "bright" images. Bottom panel is a plot of error rate - defined to be the measured overlap between the distributions compared to the number of measurements - as a function of number of pixels used (in blue); as well as the separation measure from Eq. (5.2) as a function of number of pixels used. The separation is unity or larger if the distributions do not overlap, corresponding to 0 measurable error rate. For this measurement, both of these happen when taking the 9 brightest pixels. However, separation is optimal at  $\sim 30 - 40$  brightest pixels used, where this value usually saturates.

## Multi-ion detection

For a multi-ion case, the aforementioned procedure is performed for every ion in the chain independently, the only exception being that each pixel in the image is allocated to one specific ion. The allocation is done by finding the ion centers on the image, and enlisting each pixel to its nearest ion center. Once this is done the procedure proceeds as before, with the pool of pixels for each ion limited by the pre-allocation.

The multi-ion detection capabilities are demonstrated by simultaneous measurement of the states of all ions in a 3 ion chain while performing Rabi oscillations between the "bright" and "dark" states. A wide-waist  $674\text{ nm}$  beam is used to drive a Rabi oscillation on all 3 ions simultaneously, at varying frequencies of the  $674\text{ nm}$  beam or at different pulse time lengths.

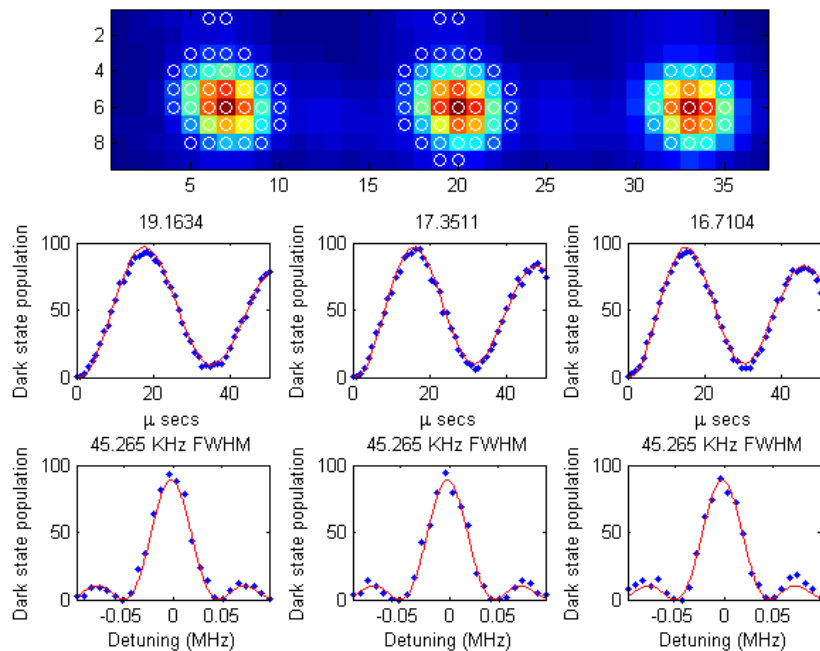


**Figure 5.8 - Multi ion detection.** Top row shows pixels allocated to each ion. Middle row is a global beam Rabi oscillation of the 3-ion chain. Quadrupole transition laser is pulsed at different time spans and ion "dark" population is measured (200 repetitions per point), illustrating the oscillation. Bottom row is a three-ion Rabi spectroscopy measurement. The pulse time span is kept constant and laser frequency is varied. Dark state population is measured, showing the quadrupole  $674\text{ nm}$  transition peak.

## Multi-ion detection crosstalk

The finite size of the ion PSF leads to unwanted detection crosstalk between ions. This problem is amplified by aberrations. If an ion is in a dark state while its neighbor is bright, Fluorescence from the neighbor ion may be enough to instigate a false "bright" detection. Although a direct measurement of the detection crosstalk has not yet been performed,

predicting detection crosstalk damage is possible. In the measurement shown in Figure 5.9 an additional “bright” ion is artificially planted in the set of “dark” images at different distances from the measured ion. The discrimination procedure is then undertaken for each inter-ion distance and the optimal results are recorded. The measurement shows detection fidelity remains high for small inter-ion distances. For 1 msec exposure times and inter ion distances of  $d > 1.6 \mu\text{m}$ . error rates - evaluated as the ratio of measured false events to the total number of measurements - are  $< 1 \times 10^{-3}$ , dropping to  $< 10^{-4}$  for  $d > 1.9 \mu\text{m}$ .

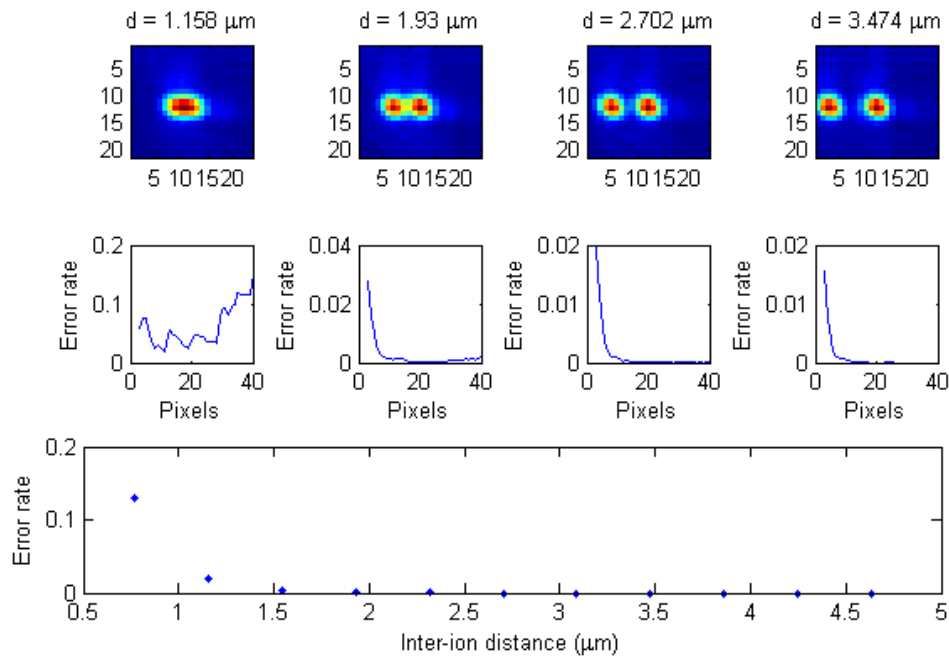


**Figure 5.9 – Detection crosstalk characterization.** Detection crosstalk is characterized by artificially planting a “bright” ion next to the dark, measured ion. Top row illustrates the distance between the measured ion (center) and the planted ion. Middle row shows error rate as a function of number of pixels used for detection. Crosstalk introduces a tighter constrain on pixel use, achieving optimal results at  $\sim 20 - 25$  pixels. Bottom row shows error rate as a function of inter ion distance for the optimal pixel register. Error falls below  $10^{-3}$  at  $1.6 \mu\text{m}$  and under  $10^{-4}$  at  $1.9 \mu\text{m}$ .

## Individual Ion Addressing

In this chapter we show and characterize the individual addressing capabilities of the IIA module, utilizing the tightly focused 674 nm narrow linewidth laser steered by two acousto-optic deflectors.

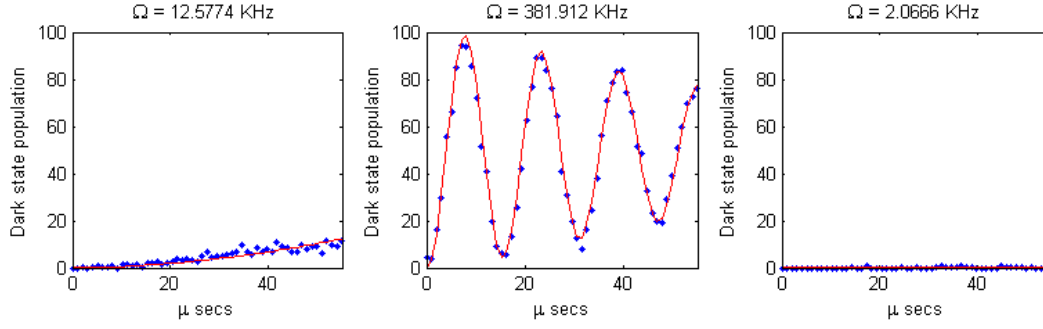
### Individually addressed Rabi oscillations

The salient parameter of an individual addressing system is the fidelity with which it can execute rotations on a selected qubit and the amount of unwanted addressing crosstalk it produces, i.e. the amount of deviation of the state of a neighbor qubit in the register from the desired unperturbed state. High crosstalk implies a low fidelity when attempting to perform single-qubit operation in a register. One measure of the crosstalk is  $\epsilon_i = \max\left(\frac{\Omega_{i-1,i+1}^i}{\Omega_i}\right)$ , the ratio of the unwanted Rabi frequencies of neighbor ions to the Rabi frequency of the addressed ion. For low enough ratios  $\left(\frac{\Omega_{i-1,i+1}^i}{\Omega_i} \ll 1\right)$ , the fidelity  $f_{i+1}$  of the neighbor ion state, after an addressing operation on ion  $i$ , is  $f \cong 1 - \epsilon_i^2$ . If, for example, an addressed operation is performed on ion  $i$  for a duration  $\tau = \frac{\pi}{2\Omega_i}$  (a " $\pi/2$ " pulse), the fidelity of the state of the neighboring ion  $i + 1$  is:

$$(6.1) \quad f_{i+1} = |\langle \text{initial state}_{i+1} | \text{final state}_{i+1} \rangle|^2 = 1 - \sin^2\left(\frac{\Omega_{i+1}^i \tau}{2}\right) =$$

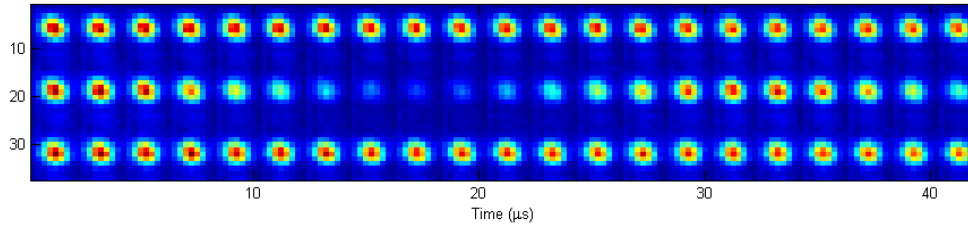
$$1 - \sin^2\left(\frac{\Omega_{i+1}^i \pi}{4\Omega_i}\right) \approx 1 - \left(\frac{\Omega_{i+1}^i \pi}{4\Omega_i}\right)^2 \cong 1 - \epsilon_i^2$$

Figure 5.1 demonstrates individual addressing of a single ion in a three ion chain, with the ions spaced 5  $\mu\text{m}$  away. The beam position maximizes the Rabi frequency of the center ion. Aberrations of the beam waist account for an asymmetry of the left and right neighbor crosstalk, which vary significantly. These measurements indicate a crosstalk error of  $\epsilon \cong 0.033$ , and thus suggest a possibility of reaching fidelities of  $\sim 0.999$ , on par with estimates of fidelity thresholds for fault-tolerant quantum computing. Further diminishing of crosstalk is achievable, for which two avenues will be pursued: a) correcting beam aberrations with improved optical alignment and/or a spatial light modulator (SLM); b) employing the addressing beam as an AC Stark shift inducer, instead of its use as an on-resonance Rabi oscillation driver (Hempel, 2014). Through the first method, the waist aberration causing the crosstalk asymmetry and creating the majority of crosstalk can be reduced. The second



**Figure 6.1 - Rabi oscillations of an addressed ion in a 3 ion chain.** Addressing middle ion with the individual addressing beam induces oscillations at  $\Omega = 382 \text{ KHz}$ . Crosstalk addressing of neighbor ion is evident, with crosstalk error  $\epsilon_2 = \frac{12.6}{382} \cong 0.033$ . Asymmetric crosstalk is likely a result of beam waist aberrations. Ions are spaced  $5.04 \mu\text{m}$  apart.

method involves applying unitary operations on the addressed ion by pulse sequences of an on-resonance global beam (addressing the entire register) and a far off-resonance individual addressing beam. The benefit of this latter method is that while for on resonance addressing  $\Omega_{Rabi} \sim |E|$ , AC Stark shift addressed sequences have a Rabi frequency proportional to the intensity,  $\Omega_{Rabi} \sim |E|^2$ , effectively narrowing the addressing beam and reducing the crosstalk from  $\epsilon$  to  $\epsilon^2$ . These methods are expected to improve fidelities to  $f > 1 - 10^{-4}$  even for shorter inter-ion distances.



**Figure 6.2 - Time lapse image of individually addressed Rabi oscillation in a 3-ion chain.** This image showcases the main capabilities of the module: imaging of the ion chain, and individual addressing of an ion in the chain. The X-axis represents the time lapse in discrete jumps, each 3-ion image corresponding to a point in time. The central ion completes more than a full Rabi oscillation while peripheral ions are untouched. Ions are spaced  $5.04 \mu\text{m}$  apart.

## Spatial control of individual addressing beam

Precise spatial control of the tightly focused beam is necessary for the addressing of different ions in a time sequence. The IIA module uses two Isomet OAD948-633 AODs for this purpose, controlling the position of the waist by applying suitable RF frequencies to the AODs. Figure 5.2 demonstrates beam control by using the laser to create an image of the ion chain via induced Rabi oscillations. The RF frequencies of the X-axis and Y-axis AODs are scanned through a  $4 \text{ MHz}$  span with a  $200 \text{ KHz}$  resolution each. Each combination of frequencies corresponds to a position of the addressing beam waist on a plane containing the ion chain. The addressing beam is then turned on for a predetermined amount of time  $\tau_s$ , and the population transferred to the dark state is recorded individually for each ion.  $\tau_s$  is chosen

to be short, such that no ion will undergo full population transfer. The result is an image of population shelving as a function of AOD frequencies for each ion, which when added together comprises a Rabi frequency image of the ion chain.

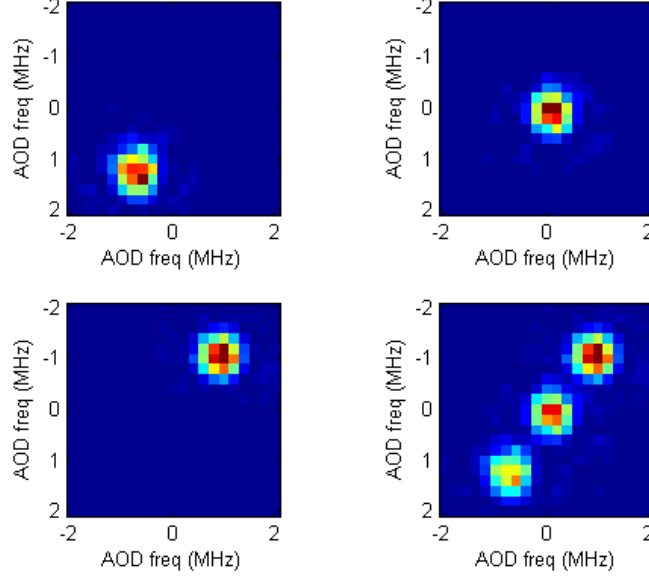


**Figure 6.3 -- Ion imaging with Rabi oscillations.** X and Y AOD frequencies are scanned over 4 MHz at 0.2 MHz resolution. For each frequency pair, which coincides with a beam position, dark state population is measured for each ion. Shelving time is  $\tau_s = 4 \mu\text{s}$ , ion distance is  $5.04 \mu\text{m}$

The addressing beam scan allows for a measurement of the correspondence between AOD frequency and ion chain distance. Ion centers are differentiated by  $7.08(8)$  pixels which correspond to  $1.42(2) \text{ MHz}$  AOD frequency. Since the ion are separated by  $5.04 \mu\text{m}$ , the correspondence is  $3.56(6) \frac{\mu\text{m}}{\text{MHz}}$ . AOD bandwidth is  $45 \text{ MHz}$ , and so the AODs should be able to scan the ion chain at a full length of  $160 \mu\text{m}$ .

Rabi oscillation mapping can also be used to characterize the beam waist, as shown in Figure 5.3. From the dark state population map one can derive a map of position-dependent Rabi frequencies, which are linearly dependent on the amplitude of the electric field induced by the laser. Analysis of the beam waist shows a field amplitude FWHM of  $3.07(6) \mu\text{m}$ , which implies an intensity FWHM of  $2.15(4) \mu\text{m}$ . The resolution is thus  $N \sim 74.5$ , similar to the expected figure.

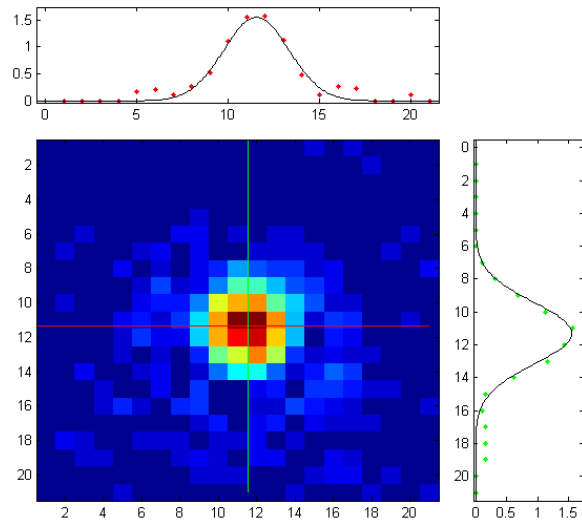


**Figure 6.4 – Addressing beam waist characterization.** A Rabi frequency mapping of the beam waist derived from the dark state shelving map shown in Figure 2. Gaussian FWHMs along X and Y axes are **3.00**, **3.14  $\mu\text{m}$**  respectively.

## Summary and outlook

Ion traps are unique in their ability to provide a high degree of control of quantum matter and therefore are prime candidates for construction of a quantum computer. For quantum computation to be feasible, coherently addressing single ions in the trap and detection without ambivalence of the ion chain state is mandatory and must be done with low error rates. For this purpose a module for individual addressing and imaging of ions was built and added upon an existing ion trapping apparatus for  $^{88}\text{Sr}^+$  ions.

non-ambivalent detection is done by imaging the ion chain onto a fast EMCCD camera. A 0.34 NA objective placed  $\sim 30.7\text{ mm}$  from the ions images the ions directly onto the camera at a distance of  $\sim 1250\text{ mm}$ , creating a magnification of  $\times 41.48(42)$ . The imaging system has a PSF with a FWHM of  $\sim 1.4 - 1.5\ \mu\text{m}$ . Camera readout while externally controlling exposure can be as low as  $\sim 0.8\text{ msec}$  after end of exposure for a large ion chain. State detection is done by calibrating the optimal number of pixels that are readout, and comparing the total signal over these pixels to a threshold. For an exposure time of  $1\text{ msec}$  the false detection rate for a single ion is substantially under  $10^{-4}$ . For multiple ions detection crosstalk is substantial only at distances smaller than  $1.9\ \mu\text{m}$ , for which crosstalk induced errors are on the order of  $10^{-4}$ .

Individual addressing is done by focusing a  $674\text{ nm}$  laser onto a single ion in order to drive the quadrupole-allowed  $5S_{\frac{1}{2}} \leftrightarrow 4D_{\frac{5}{2}}$  transition coherently. The laser is steered by two AODs in an XY configuration. The beam is focused through the objective to a  $2.15\ \mu\text{m}$  spot at FWHM of the intensity. Oscillations are induced by resonant drive of the carrier transition. For ions at a distance of  $\sim 5\ \mu\text{m}$  the crosstalk-induced neighbor-ion Rabi frequency is 3.3% of the addressed ion Rabi frequency, allowing for errors of  $\sim 10^{-3}$ . Most of the crosstalk is due to an aberration causing asymmetry of the beam shape. Fidelity should be significantly improved with future methods.

## Outlook

Several upgrades are planned for the system, which can significantly augment its abilities:

- i. **Dedicated detection FPGA:** Currently state inference occurs off-line by MATLAB. A dedicated FPGA will enable a live readout of the camera data via the CameraLink output of the Andor iXon. The FPGA will capture an image and perform simple data analysis in order to determine the state of the ion array, hopefully in a time much

shorter than 1 msec. The state of the array will then be fed to the experiment-controlling FPGA, which will make a real-time decision on the following pulse sequence according to the state of the ions. Such architecture will grant ability to perform quantum error correcting codes.

- ii. **Individual addressing with AC Stark shifts:** a procedure for individual addressing, already demonstrated in other labs, that utilizes the individual addressing beam for AC Stark shifts instead of carrier Rabi oscillations, by detuning the frequency far from resonance. This procedure should significantly decrease crosstalk.
- iii. **Shaping the addressing beam with a Spatial Light Modulator (SLM):** with an SLM one can electronically control the shape of the addressing beam waist to a high resolution. As a first mission, the SLM can be used to diminish aberrations and tighten the beam waist to the diffraction limited size, hence significantly decreasing crosstalk. Further along, perhaps it can also be used to engineer interesting or convenient beam shapes that differ from a diffraction-limited spot.

## Bibliography

- Acton, M., Brickman, K.-A., Haljan, P., Lee, P., Deslauriers, L., Monroe, C., 2006. Near-perfect simultaneous measurement of a qubit register. *Quant. Inf. Comp.* 6, 465.
- Akerman, N., Kotler, S., Glickman, Y., Keselman, A., and Ozeri, R., 2012. Quantum control of  $88\text{Sr}^+$  in a miniature linear Paul trap. *App. Phys. B: Lasers and Optics*, 107, 1167-1174.
- Barrett, M. D., Chiaverini, J., Schaetz, T., Britton, J., Itano, W. M., Jost, J. D., Knill, E., Langer, C., Leibfried, D., Ozeri, R., Wineland, D. J., 2004. Deterministic quantum teleportation of atomic qubits. *Nature* 429, 737–739.
- Bergquist, J. C., Hulet, R. G., Itano, W. M., Wineland, D. J., 1986. Observation of quantum jumps in a single atom. *Phys. Rev. Lett.* 57 (14), 1699–1702.
- Burrell, H., Szwer, D. J., Webster, S. C., and Lucas, D. M. 2010. Scalable simultaneous multi-qubit readout with 99.99% single-shot fidelity. *Phys. Rev. A*, 81:04030.
- Chiaverini, J., Britton, J., Leibfried, D., Knill, E., Barrett, M. D., Blakestad, R. B., Itano, W. M., Jost, J. D., Langer, C., Ozeri, R., Schaetz, T., Wineland, D. J., 2005. Implementation of the semiclassical quantum Fourier transform in a scalable system. *Science* 308, 997–1000.
- Chiaverini, J., Leibfried, D., Schaetz, T., Barrett, M. D., Blakestad, R. B., Britton, J., Itano, W. M., Jost, J. D., Knill, E., Langer, C., Ozeri, R., Wineland, D. J., 2004. Realization of quantum error correction. *Nature* 432, 602–605.
- Cirac, J. I., Zoller, P., 1995. Quantum computations with cold trapped ions. *Phys. Rev. Lett.* 74 (20), 4091–4094.
- Dehmelt, H. G., 1975. Proposed  $10^{14} \delta\nu < \nu$  laser fluorescence spectroscopy on  $\text{Ti}^+$  mono-ion oscillator II (spontaneous quantum jumps). *Bull. Am. Phys. Soc.* 20, 60.
- Deutsch, D. & Jozsa, R., 1992. Rapid solution of problems by quantum computation. *Proc. R. Soc. Lond.* A439, 553–558.
- Deutsch, D., 1985. Quantum theory, the Church-Turing principle and the universal quantum computer. *Proc. R. Soc. London A* 400, 97.

- DiVincenzo, D. P., 1997. Topics in Quantum Computers, in Mesoscopic Electron Transport, (ed. Kowenhoven, L., Schön, G. & Sohn, L.), NATO ASI Series E, (Kluwer Ac. Publ., Dordrecht,)
- DiVincenzo, D. P., 2000, “The physical implementation of quantum computation,” Fortschr. Phys. 48, 771–783.
- Feynman, R., 1982. Simulating physics with computers. Int. J. Theoret. Phys. 21, 467.
- Haljan, P. C., Lee, P. J., Brickman, K.-A., Acton, M., Deslauriers, L., Monroe, C., 2005. Entanglement of trapped-ion clock states. Phys. Rev. A 72, 062316.
- Hempel, C., 2014. Digital quantum simulation, Schrodinger cat state spectroscopy and setting up a linear ion trap. PhD thesis, Leopold-Franzens-Universität Innsbruck.
- Hensinger, W. K., Olmschenk, S., Stick, D., Hucul, D., Yeo, M., Acton, M., Deslauriers, L., Monroe, C., 2006. T-junction ion trap array for twodimensional ion shuttling storage, and manipulation. Appl. Phys. Lett. 88, 034101.
- Hume, D. B., Rosenband, T., Wineland, D. J., 2007. High-fidelity adaptive qubit detection through repetitive quantum nondemolition measurements. Phys. Rev. Lett. 99 (12), 120502.
- James, D. F. V., 1998. Quantum dynamics of cold trapped ions with application to quantum computation. Appl. Phys. B 66, 181.
- Johanning M., Braun A., Timoney N., Elman V., Neuhauser W. & Wunderlich C., 2009. Individual addressing of trapped ions and coupling of motional and spin states using rf radiation. Phys. Rev. Lett. 102(7), 073004.
- Keselman, Y. Glickman, N. Akerman, S. Kotler, and R. Ozeri, 2011. High-fidelity state detection and tomography of a single-ion Zeeman qubit. New J. Phys. 13, 073027.
- Knoernschild, X. L. Zhang, L. Isenhower, A. T. Gill, F. P. Lu, M. Saffman, and J. Kim, 2010. Independent individual addressing of multiple neutral atom qubits with a MEMS beam steering system. [physics.atom-ph] p. arXiv:1006.2757v1.
- Leibfried, D., 1999. Individual addressing and state readout of trapped ions utilizing micromotion, Phys. Rev. A 60, 3335.

- Merrill, J. T., Doret, S. C., Vittorini, G., Addison, J., Brown, K. R., 2014. Transformed composite sequences for improved qubit addressing. *Phys.Rev.A* 90, 040301.
- Mintert, F., Wunderlich, C., 2001. Ion-trap quantum logic using longwavelength radiation. *Phys. Rev. Lett.* 87 (25), 257904.
- Monroe, C., Meekhof, D. M., King, B. E., Itano, W. M., Wineland, D. J., 1995. Demonstration of a fundamental quantum logic gate. *Phys. Rev. Lett.* 75 (25), 4714–4717.
- Myerson, A. H., Szwer, D. J., Webster, S. C., Allcock, D. T. C., Curtis, M. J., Imreh, G., Sherman, J. A., Stacey, D. N., Steane, A. M., Lucas, D. M., 2008. High-fidelity readout of trapped-ion qubits. *Phys. Rev.Lett.* 100, 200502.
- Nagerl, H. C., D. Leibfried, H. Rohde, G. Thalhammer, J. Eschner, F. Schmidt-Kaler, and R. Blatt, 1999. Laser addressing of individual ions in a linear ion trap. *Phys. Rev. A* 60, 145
- Nagourney, W., Sandberg, J., Dehmelt, H., 1986. Shelved optical electron amplifier: Observation of quantum jumps. *Phys. Rev. Lett.* 56 (26), 2797– 2799.
- Navon, N., Kotler, S., Akerman, N., Glickman Y., Almog I., and Ozeri, R., 2013. Addressing two-level systems variably coupled to an oscillating field. *Phys. Rev. Lett.*, 111, 073001.
- Piltz, C., Sriarunothai, T., Var´on, A.F., and Wunderlich, C. 2014. A trapped-ion-based quantum byte with 10– 5 next-neighbor cross-talk. *Nat. Commun.* 5, 4679.
- Roos, C. F., Riebe, M., Haffner, H., Hansel, W., Benhelm, J., Lancaster, G. P. T., Becher, C., Schmidt-Kaler, F., Blatt, R., 2004. Control and measurement of three-qubit entangled states. *Science* 304 (5676), 1478–1480.
- Rowe, M. A., Ben-Kish, A., DeMarco, B., Leibfried, D., Meyer, V., Beall, J., Britton, J., Hughes, J., Itano, W. M., Jelenkovi´c, B., Langer, C., Rosenband, T., Wineland, D. J., 2002. Transport of quantum states and separation of ions in a dual RF ion trap. *Quant. Inf. Comp.* 2, 257–271.
- Sauter, T., Neuhauser, W., Blatt, R., Toschek, P. E., 1986. Observation of quantum jumps. *Phys. Rev. Lett.* 57 (14), 1696–1698.

Scheunemann, R., Cataliotti, F.S., Hansch, T. W. , and Weitz, M., 2000. Resolving and addressing atoms in individual sites of a CO<sub>2</sub>-laser optical lattice. *Phys. Rev. A* 62, 051801

Shor, P. W., 1994. Algorithms for quantum computation: discrete logarithms and factoring. In: *Proceedings of the 35th Annual Symposium on Foundations of Computer Science*, Santa Fe, NM, Nov. 20-22, IEEE Computer Society Press, pp. 124–134.

Staanum, P., Drewsen, M., 2002. Trapped-ion quantum logic utilizing position dependent ac-Stark shifts. *Phys. Rev. A* 66, 040202.

Turchette, Q., Wood, C., King, B., Myatt, C., Leibfried, D., Itano, W., Monroe, C., Wineland, D., 1998. Deterministic entanglement of two ions. *Phys. Rev. Lett.* 81, 3631.

U. Warring, C. Ospelkaus, Y. Colombe, R. Jordens, D. Leibfried, and D. Wineland, 2013. Individual-ion addressing with microwave field gradients. *Phys. Rev. Lett.* 110, 173002.

Wang, S. X. Labaziewicz, J. Ge, Y. Shewmon, R. & Chuang, I. L., 2009. Individual addressing of ions using magnetic field gradients in a surface-electrode ion trap. *Appl. Phys. Lett.* 94, 094103.

Weitenberg, M. Endres, J. F. Sherson, M. Cheneau, P. Schausz, T. Fukuhara, I. Bloch, and S. Kuhr, 2011. Single-spin addressing in an atomic Mott insulator. *Nature* 471, 319.